Cancer Letters 661 (2026) 218848

Contents lists available at ScienceDirect

Cancer Letters

journal homepage: www.elsevier.com/locate/canlet

Original Articles

Oncogenic VEGFR2 rewires the extracellular matrix to impair endothelial mechanics and destabilize tumor vasculature

Mattia Domenichini [a,b,1], Michela Corsini [a,b,1], Cosetta Ravelli [a,b], Anastasia Ricci [e], Elisa Moreschi [a], Elisabetta Grillo [a,b], Camilla Maggi [a], Gianluca Baldanzi [c], Sonia Chiodini [a,d], Diana Eveline Sanchez-Amador [d], Julia Kraxner [e], Michael G. Monaghan [d], Holger Gerhardt [e], Michele Menotta [f], Stefania Mitola [a,b,*]

[a] Department of Molecular and Translational Medicine, Università degli Studi di Brescia, Via Branze 39, Brescia, Italy
[b] Mechanobiology Research Center at UNIBS, Università degli Studi di Brescia, Italy
[c] Center for Translational Research on Allergic and Autoimmune Diseases, Department of Translational Medicine, Università del Piemonte Orientale, Novara, Italy
[d] Discipline of Mechanical, Manufacturing and Biomedical Engineering, School of Engineering, Trinity College Dublin, Dublin 2, Ireland
[e] Integrative Vascular Biology, Max Delbrück Center (MDC), Robert-Rössle-Straße 10, Berlin, Germany
[f] Department of Biomolecular Sciences University of Urbino "Carlo Bo", Via Saffi 2, Urbino, PU, 61029, Italy

ARTICLE INFO

Keywords:
Tumoral vasculature
Extracellular matrix
Mechanosensing
Endothelial-to-mesenchymal transition
Focal adhesion
Cell-cell junction

ABSTRACT

Solid tumors are highly dynamic environments, in which endothelial cells (ECs) interface with blood, cancer cells, and the extracellular matrix (ECM), thereby regulating tumor behavior and metastatic dissemination. We recently showed that aberrant Vascular Endothelial Growth Factor Receptor 2 (VEGFR2) activation promotes tumor progression through ECM remodeling. Here we investigated whether VEGFR2-driven ECM remodeling affects EC behavior and vessel stability.

Using decellularized ECM from Sk-Mel-31 melanoma cells expressing either $VEGFR2^{WT}$ or the aberrant $VEGFR2^{R1032Q}$ mutant, we found that $VEGFR2^{R1032Q}$ reshapes ECM composition, including core matrisome components, ECM-modifying enzymes, and vascular-associated proteins. ECs seeded on $VEGFR2^{R1032Q}$-derived ECM displayed altered adhesion dynamics, characterized by focal adhesion remodeling, increased haptotaxis, and impaired morphogenic capacity. This remodeled ECM also induced cytoskeletal reorganization and, disruption of VE-cadherin junctions via RhoA activation. Consistently, $VEGFR2^{R1032Q}$-derived tumors exhibited more immature vessels with discontinuous junctions and the expression of mesenchymal markers. Under laminar flow, ECs exposed to $VEGFR2^{R1032Q}$-ECM showed a delayed calcium dynamic, altered YAP localization, defective polarization, actin alignment and impaired shear-stress adaptation.

Overall, these findings identify VEGFR2-driven ECM remodeling as a non-cell-autonomous mechanism that destabilizes tumor vasculature by impairing endothelial adhesion, mechanosensing, and junctional integrity, highlighting tumor/ECM/endothelium crosstalk as a potential therapeutic vulnerability.

1. Introduction

Solid tumors are complex ecosystems characterized by the bulk core of tumor cells surrounded by an interactive network of non-cancerous cells, extracellular matrix (ECM) and blood vessels, collectively known as the tumor microenvironment (TME) [1]. In tumors, the TME dynamically interacts with cancer cells sustaining their growth, survival and dissemination capacities [2]. In this context, the ECM plays multiple crucial roles, including a structural scaffold for cells, modulation of the microenvironment, and reservoir of soluble molecules and growth factors [3]. ECM also acts as both a mechanical and biochemical platform for endothelial cells (ECs), which continuously integrate matrix-derived and hemodynamic cues to maintain vascular homeostasis. Integrins transduce ECM signaling inside ECs promoting the assembly and maturation of focal adhesions (FAs), physically associated to the actin cytoskeleton [4]. Through focal adhesion-associated signaling and

* Corresponding author. Department of Molecular and Translational Medicine, Università degli Studi di Brescia, Via Branze 39, Brescia, 25123, Italy.
E-mail address: stefania.mitola@unibs.it (S. Mitola).
[1] Authors equally contributed.

https://doi.org/10.1016/j.canlet.2026.218848
Received 7 May 2026; Received in revised form 28 August 2026; Accepted 16 September 2026
Available online 24 September 2026
0304-3835/© 2026 The Authors. Published by Elsevier B.V. This is an open access article under the CC BY license (http://creativecommons.org/licenses/by/4.0/).

RhoA-dependent actomyosin contractility, variations in ECM can therefore regulate intracellular tension and cytoskeletal organization. These forces are transmitted across the endothelial monolayer through adherens and tight junctions, which control endothelial barrier integrity [4]. In parallel, blood flow-derived shear forces contribute to the vascular homeostasis, and further modulate cytoskeletal remodeling, cell polarity and junctional stability [5]. Altogether, vascular function relies on the coordinated integration of basal, lateral and apical mechanical cues. In tumors, disruption of this balance impairs endothelial mechanotransduction leading to the formation of structurally and functionally abnormal, leaky blood vessels. Thereby these forces influence tumor growth and dissemination [6].

Vascular endothelial growth factor receptor 2 (VEGFR2) is a tyrosine kinase not only related to tumor vasculature development, but also involved in cancer cell survival, proliferation and migration. The R1032Q substitution is the most frequently reported VEGFR2 mutation in cancer patients (cBioPortal for Cancer Genomics 04/16/2026). It sustains tumor growth and dissemination by heterodimerizing with the wild-type receptor [7]. Importantly, the expression of VEGFR2^{R1032Q} increases the sensitivity to tyrosine kinase inhibitors, including

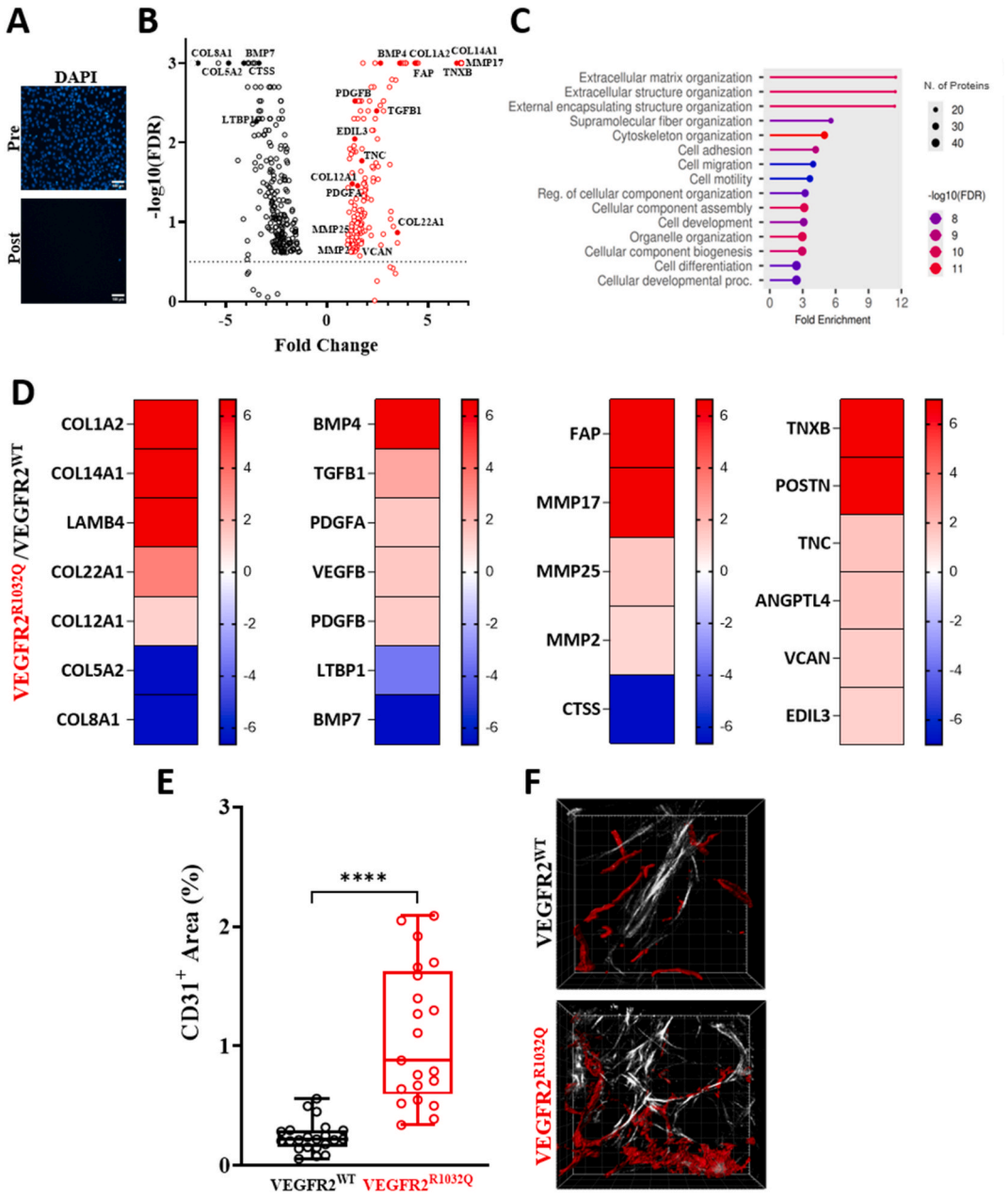


Fig. 1. Characterization of dECM from VEGFR2^{WT} Sk-MEL-31- and VEGFR2^{R1032Q} Sk-MEL-31-derived tumors. A) DAPI stain of Sk-Mel-31 monolayer pre- and post-decellularization, scale bar 100 μm; B) Vulcano plot of differentially expressed proteins in VEGFR2^{R1032Q} and VEGFR2^{WT} dECMs, upregulated (in red) and downregulated (in black) proteins. Dashed line indicates the significance threshold. Labelled proteins belong to ECM-core proteins, ECM-modifying enzymes and ECM-related growth factors (n = 2). C) Pathway enrichment of differentially expressed proteins performed with ShinyGO 0.85. Bubble size represents the number of proteins involved in the pathway and the color indicates the significance. D) Heatmap of selected ECM-related proteins differentially expressed in VEGFR2^{R1032Q} Sk-MEL-31-derived tumors compared to VEGFR2^{WT} Sk-MEL-31-derived ones. E) Quantification of CD31^{+} area in VEGFR2^{R1032Q} Sk-MEL-31- and VEGFR2^{WT} Sk-MEL-31-derived tumors. Single data are represented as empty dots ± Standard Deviation. 4-5 different fields were analyzed in 5 independent samples. ****, $p < 0.001$, unpaired Student's t-test. F) Representative CD31 staining and Second harmonic generation (SHG) imaging of collagen fibers in Sk-MEL-31-derived tumors, scale bar 50 μm.

cabozantinib and lenvatinib, supporting the potential therapeutic relevance of this alteration [8].

Beyond its canonical functions, aberrant VEGFR2 activation regulates mechanotransduction in melanoma, ovarian, and breast cancers cells, integrating mechanical and soluble cues from the extracellular environment and modulating the intracellular mechanosensing [9–11]. In this context, VEGFR2^{R1032Q} signaling remodels ECM composition, organization and mechanical properties through PI3K-AKT and ERK pathways. Accordingly, normalization or pharmacological inhibition of VEGFR2 activity restores ECM architecture, highlighting VEGFR2 as a key regulator of ECM dynamics and tumor mechanics [11]. Despite these observations, whether aberrant VEGFR2-driven ECM remodeling directly affects endothelial behavior and vascular function remains poorly understood.

Here, we demonstrate that ECM produced by tumor cells harboring VEGFR2^{R1032Q} profoundly alters endothelial mechanosensing and vascular stability. Specifically, VEGFR2-dependent ECM remodeling reshapes endothelial adhesion dynamics, cytoskeletal organization, cell-cell junction integrity and its response to shear stress contributing to vascular dysfunction. These findings identify ECM-mediated tumor-endothelium crosstalk as a critical regulator of vascular instability and a potential therapeutic vulnerability.

2. Results

2.1. Aberrant VEGFR2 modulates ECM composition and interaction with the tumor vessels

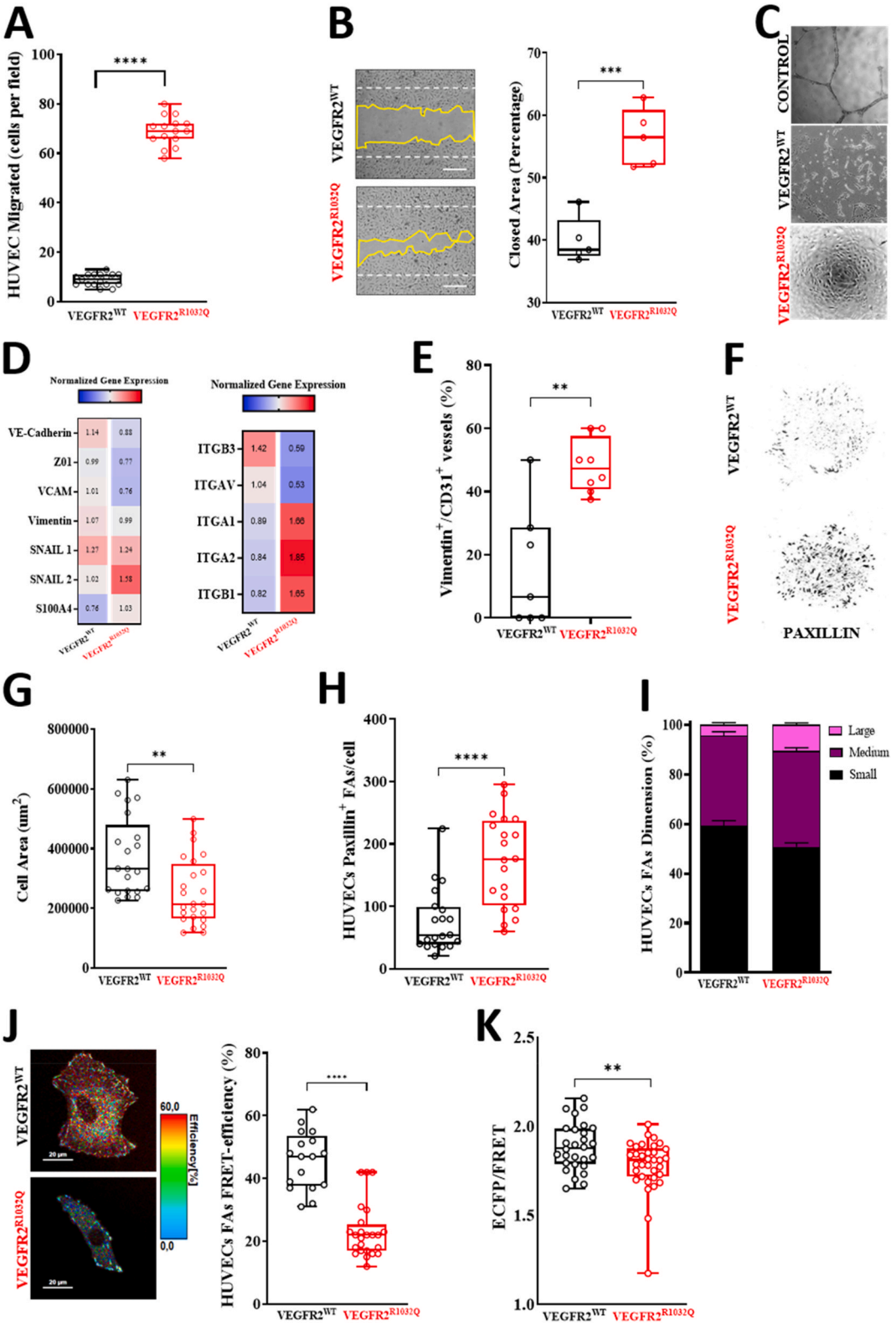
To investigate how aberrant VEGFR2 activation alters TME and affects vascular organization, we used the VEGFR2^{R1032Q} mutant as a model of VEGFR2 activation [7]. We produced a decellularized ECM (dECM) from VEGFR2^{WT} Sk-Mel-31 and VEGFR2^{R1032Q} Sk-Mel-31 cells as previously shown [11]. Successful decellularization was confirmed by the absence of DAPI-positive nuclei (Fig. 1A). The resulting VEGFR2^{WT}- and VEGFR2^{R1032Q}-dECMs were subsequently subjected to mass spectrometry-based proteomic analysis to obtain an unbiased, discovery-level characterization of the matrisome. Identified proteins were first filtered based on their extracellular localization to exclude cellular and environmental contaminants. Subsequent analysis included only significantly dysregulated proteins ($p < 0.05$) showing at least a two-fold increase or decrease in abundance. Based on these criteria, 1231 proteins were identified as differentially expressed in VEGFR2^{R1032Q} Sk-Mel-31 dECM compared to VEGFR2^{WT} Sk-Mel-31 dECM (Supplementary Table 1). Among them, 834 were downregulated, while 397 were upregulated (Fig. 1B). Gene Ontology enrichment analysis, performed with ShinyGO 0.85, confirmed that the most significantly affected pathways were associated with extracellular matrix organization and extracellular structure organization (Fig. 1C). Detailed analysis of the individual molecules identified in the matrices further demonstrated that ECM composition was altered at multiple levels, from structural ECM components like collagens and laminin chains, to ECM-modifying enzymes and ECM-associated signaling molecules, as shown in Fig. 1D. Among core ECM proteins COL1A2, COL14A1, COL22A1, COL12A1, LAMB4 were more expressed in VEGFR2^{R1032Q} Sk-Mel-31 dECM, while COL5A2 and COL8A1 were less expressed. This pattern was accompanied by significant modulation of proteins involved in ECM dynamics. Among them, metalloproteases MMP2, MMP17, MMP25 were overexpressed in the mutant condition, and the Fibroblast Activating Protein (FAP), which mediates proteolytic process of collagen fibers after MMPs cleavage [9], was similarly increased. Conversely, other ECM-remodeling proteins like Cathepsins (CTSS, CTSL) were expressed at lower levels in the mutant-derived ECM. Consistent with these changes, several ECM-associated growth factors, including TGFB1, LTBP1, VEGFB, PDGFA, PDGFB, BMP4, BMP7 were differentially expressed between the two conditions (Fig. 1D). The altered expression of these molecules, particularly TGFB1 and its regulators LTBP1, BMP4/7, and PDGFA/B, may modulate collagen biosynthesis and deposition, as well as MMPs activity, consequently influencing ECM fibrosis, stiffness, and overall structural organization. Together, these data highlight a broad impact of the VEGFR2^{R1032Q} mutation on both ECM structure and the signaling environment.

In addition, glycoproteins and proteoglycans involved in vascular remodeling [12], including tenascin C (TNC), tenascin X (TNXB), VCAN, EDIL3, POSTN, and ANGPTL4 were significantly dysregulated, indicating a shift toward a pro-angiogenic and immature vascular phenotype identified by proteomic analysis (Fig. 1D). TNC and TNXB regulate ECM assembly and stiffness, interacting with core-ECM proteins [13]. Their aberrant expression regulates ECM digestion and fibrosis, in turn promoting vascular remodeling and endothelial-to-mesenchymal transition (EndMT) [14]. Along with high VCAN expression, increased levels of EDIL3, POSTN, and ANGPTL4 promote vessel formation leading to a high vessel density and immature vasculature [15–18]. To assess the *in vivo* relevance of these findings, VEGFR2^{WT} Sk-Mel-31 and VEGFR2^{R1032Q} Sk-Mel-31 were subcutaneously injected in NOD/SCID mice. In line with our previous results [11], the expression of VEGFR2^{R1032Q} enhanced tumor growth. VEGFR2^{WT} Sk-Mel-31- and VEGFR2^{R1032Q} Sk-Mel-31-derived tumors were then analyzed to evaluate how ECM architecture interfaces with the vascular network. VEGFR2^{R1032Q} Sk-Mel-31-derived tumors showed a higher vascularization as demonstrated by the CD31^{+} staining (Fig. 1E). Second harmonic generation (SHG) imaging revealed that VEGFR2^{R1032Q} expression induced structural ECM remodeling, as demonstrated by the reduced orientation of collagen fibers (Fig. 1D) [11]. Of note, collagen fibers in VEGFR2^{R1032Q} Sk-Mel-31-derived tumors, supported and closely associated with the vascular network. In contrast, these associations were limited in VEGFR2^{WT} Sk-Mel-31 tumors (Fig. 1F). These observations highlighted a distinct TME architecture driven by the expression of VEGFR2^{R1032Q}. Taken together, these data revealed that the VEGFR2^{R1032Q} Sk-Mel-31 ECM undergoes profound structural and functional remodeling, which in turn reshapes vessel formation, maturation, and performance likely through both mechanical and biochemical mechanisms. The proteomic analysis identified several candidate proteins potentially associated with the expression of VEGFR2^{R1032Q}; however, because their differential abundance was not independently confirmed using orthogonal protein-based approaches, candidate-specific findings should be considered exploratory.

2.2. Remodeled ECM influences endothelial mechanics and functional plasticity

To assess how the ECM produced by the two isogenic cell lines influenced EC behavior, we evaluated endothelial responses to VEGFR2^{WT}- or VEGFR2^{R1032Q} -dECMs. Haptotaxis assay revealed that VEGFR2^{R1032Q} dECM significantly enhanced EC migration compared to VEGFR2^{WT} dECM (Fig. 2A). This increased migratory propensity was confirmed by scratch assay in which ECs directly adhered on VEGFR2^{R1032Q} dECM (Fig. 2B).

Despite enhanced migration, ECs seeded on VEGFR2^{R1032Q} -dECM exhibited a marked impairment of morphogenesis. In tube formation assays, ECs formed vascular-like structures on control matrices, while VEGFR2^{WT}-dECM partially reduced this morphogenic ability, as demonstrated by smaller and more fragmented tubular structures (Fig. 2C). In contrast, VEGFR2^{R1032Q}-dECM completely abolished tube formation, indicating a functional uncoupling between migration and morphogenic potential. Consistent with these defects, transcriptional analysis revealed alterations in the expression profiles of integrins and mesenchymal markers. ECs seeded on VEGFR2^{R1032Q}-dECM downregulated key endothelial markers such as VE-cadherin, ZO-1 and VCAM, while concurrently upregulating SNAIL1 and SNAIL2 (Fig. 2D). Also, the EC integrin repertoire shifted from the expression of αvβ3 toward α1β1 and/or α2β1 (Fig. 2D). These transcriptional changes suggested an increased endothelial plasticity and were consistent with an



(caption on next page)

Fig. 2. Gene expression and remodeled focal adhesions in ECs plated on VEGFR2^{R1032Q}-dECM. A) EC haptotatic migration performed in a Boyden's chamber. Individual data are shown as empty dots ± Standard Deviation (n = 15 from three independent experiments). ****, p < 0.001, unpaired Student's t-test. **B)** Collective migration of ECs seeded on VEGFR2^{WT}- and VEGFR2^{R1032Q}-dECMs. Representative images on the left and % covered area on the right. Individual data are shown as empty dots ± Standard Deviation (n = 5 from three independent experiments). ***, p < 0.005, Student's t-test. **C)** Tubulogenesis assay performed with ECs embedded in matrigel mixed with PBS or solubilized VEGFR2^{WT}- and VEGFR2^{R1032Q}-dECMs. Tube formation was evaluated at 18 h after seeding in two independent experiments; **D)** mRNA expression of endothelial, mesenchymal markers and integrins measured through quantitative PCR in ECs seeded for 24 h on VEGFR2^{WT}- and VEGFR2^{R1032Q}-dECMs (n = 3); **E)** Quantification of CD31^{+}/vimentin^{+} vessels in VEGFR2^{WT} Sk-Mel-31- and VEGFR2^{R1032Q} Sk-Mel-31-derived tumors (n = 5-6). **, p < 0.01, Student's t-test. **F)** Representative images of FA distribution, size and number in ECs plated on VEGFR2^{WT}- and VEGFR2^{R1032Q}-dECMs. **G)** EC area measurement. Individual data are represented as empty dots ± Standard Deviation (n = 20-24 from three independent experiments). **, p < 0.01, Student's t-test. **H)** Number of FAs in ECs plated on VEGFR2^{WT}- and VEGFR2^{R1032Q}-dECMs. Individual data are represented as empty dots ± Standard Deviation (n = 21-24 from three independent experiments).****, p < 0.001, Student's t-test. **I)** Size of FAs in ECs plated on VEGFR2^{WT}- and VEGFR2^{R1032Q}-dECMs. Individual data are represented as empty dots ± Standard Deviation (n = 21-24 from three independent experiments). **J)** Vinculin tension in FAs measured with the Vin-TS FRET-based sensor. Color-coded map represents sensor FRET efficiency in FAs. Quantification of FRET efficiency. Individual data are represented as empty dots ± Standard Deviation (n = 17-25 from two independent experiments). ****, p < 0.001, Student's t-test. **K)** FAK activity in FAs of ECs on VEGFR2^{WT}- and VEGFR2^{R1032Q}-dECMs measured with the FAT-FAK FRET-based sensor. FRET efficiency, displayed as ECFP/FRET ratio. Individual data are represented as empty dots ± Standard Deviation (n = 28-34 from two independent experiments). **, p < 0.01, Student's t-test.

early or partial EndMT-associated signature; however, they were insufficient to establish the occurrence of a complete EndMT. Given the limitations of the *in vitro* setting, particularly the 24 h experimental timeframe, we investigated whether ECs acquired mesenchymal-associated features *in vivo*. CD31/vimentin double immunofluorescence revealed a significantly higher proportion of CD31^{+} ECs co-expressing vimentin in VEGFR2^{R1032Q} Sk-Mel-31-derived tumors compared with VEGFR2^{WT} tumors (Fig. 2E and Supplementary Fig. 1).

These data prompted us to further evaluate the effect of remodeled ECM on EC adhesion. To this aim, ECs were seeded onto VEGFR2^{WT}-dECMs or VEGFR2^{R1032Q}-dECMs for 24 h, fixed and stained for paxillin to evaluate the adhesion contacts (Fig. 2F). Both dECMs were permissive for EC adhesion, and all cells were attached upon 24 h. However, VEGFR2^{R1032Q}-dECM decreased the EC spreading as demonstrated by the reduced cell area (Fig. 2G), and increased the number of paxillin^{+} FA plaques per cell (Fig. 2H). Additionally, adhesion to VEGFR2^{R1032Q}-

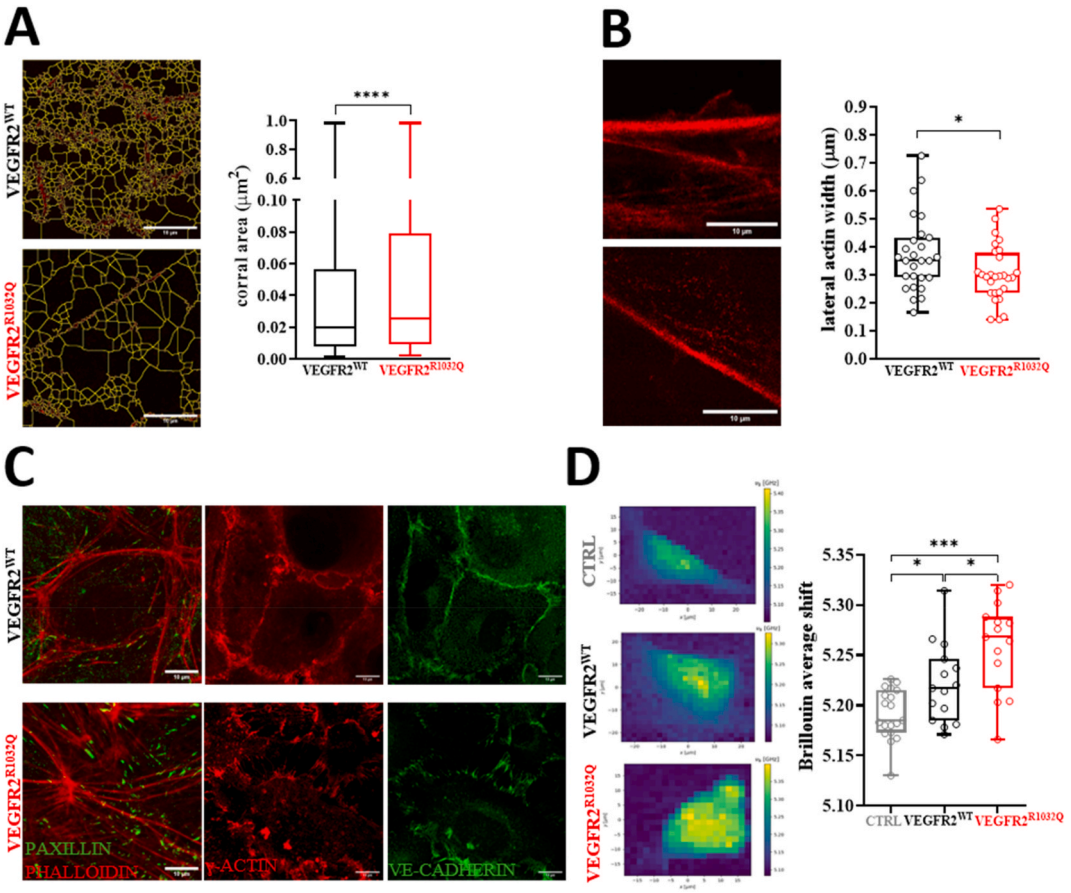


Fig. 3. Mutant VEGFR2-derived ECM affects cytoskeletal remodeling and cellular structural density. A) Representative images of corrals in ECs plated on VEGFR2^{WT}-dECM and VEGFR2^{R1032Q}-dECM (scale bar 10 μm) and quantification of corral area expressed in μm^2. Single dots are not provided due to the high number of corrals/cells. Data derived from the analysis of 27-28 cells from two independent experiments. ****, p < 0.001, Student's t-test. **B)** Representative images of lateral cortical actin (scale bar 10 μm) and quantification, expressed in μm. Individual data are represented as empty dots ± Standard Deviation (n = 27-28 cells from two independent experiments).*, p < 0.05,Student's t-test. **C)** Representative immunofluorescence images of paxillin/phalloidin, gamma-actin and VE-cadherin staining in ECs seeded on VEGFR2^{WT}- and VEGFR2^{R1032Q}-dECMs (scale bar 10 μm). **D)** Color-coded map (left) represents Brillouin shift values (GHz) in ECs plated on VEGFR2^{WT}-dECM and VEGFR2^{R1032Q}-dECM. Brillouin average shift measurements are shown in the box plot. Individual data are represented as empty dots ± Standard Deviation (n = 15-20 from four independent experiments).*, p < 0.05, ***, p < 0.005, Student's t-test.

dECM significantly increased FA size compared with that observed in ECs plated on VEGFR2^{WT}-dECM (Fig. 2I).

Consistent with this, FRET-based tension measurements revealed increased mechanical tension across vinculin in ECs on VEGFR2^{R1032Q}-dECM, indicating enhanced force transmission at adhesion sites (Fig. 2J). In parallel, FAK activity was measured within FAs by transfecting ECs with the FRET-based FAT-FAK biosensor [19]. A significant reduction in FAK activity was detected (Fig. 2K) in ECs plated on VEGFR2^{R1032Q}-dECMs. Therefore, the reduced FAK activity, together with the increased size and number of FAs, suggested that a lower FAs turnover may stabilize the EC adhesion on VEGFR2^{R1032Q}-dECM. Together, these results demonstrate that VEGFR2^{R1032Q}-driven ECM remodeling reprograms EC adhesion by promoting stable, high-tension focal adhesions with reduced turnover. This adhesive reprogramming is associated with enhanced migratory behavior, impaired morphogenesis and increased endothelial plasticity, consistent with an early EndMT-related phenotype.

2.3. Mechanical cues arising from the ECM reshape endothelial mechanotransduction-associated structures

In ECs, intracellular mechano-forces arising from FAs are converted into biochemical signals that drive cytoskeletal remodeling and junctional reorganization [4]. Given the profound changes in FA dynamics, we next investigated how VEGFR2^{R1032Q}-dECM affects cytoskeletal organization. Using expansion microscopy, we analyzed the nanoscale organization of the actin cytoskeleton in ECs seeded on VEGFR2^{WT}- or on VEGFR2^{R1032Q}-dECMs. This approach provided nanoscale visualization of actin filaments through an approximately four-fold physical enlargement of the samples. Quantitative analysis revealed a significant increase in corral area, identified as delimited compartment of actin network in the basal portion of the cell, in ECs plated on VEGFR2^{R1032Q}-dECM (Fig. 3A), indicating altered force distribution at the cell-matrix interface. The actin-mediated basal membrane compartmentalization contributed to the spatial coordination of FAs and related intracellular mechanotransduction [20]. Analysis of the lateral cortical actin further highlighted major structural differences [21]. In ECs plated on the VEGFR2^{R1032Q}-dECM the lateral actin network was thinner, highlighting a reduced actin polymerization underneath the membrane (Fig. 3B).

Also, in ECs plated on VEGFR2^{WT}-dECM, actin filaments were aligned parallel to the plasma membrane, consistent with stable mechanical support. Consistently, paxillin/phalloidin staining confirmed that focal adhesions in ECs on VEGFR2^{R1032Q}-dECM were more tightly connected to contractile actin fibers, supporting a high-tension adhesive state (Fig. 3B). This rearrangement reflected the modifications in EC adhesive properties described above and was associated with differences in FA distribution and size, as well as altered FA-actin interactions. The alterations in the overall cytoskeletal structure observed in the VEGFR2^{R1032Q} condition suggested that the cortical actin might play a key role in cell-cell junction assembly and stability [22]. Thus, ECs were stained for gamma-actin, which specifically polymerizes beneath the cell membrane [23]. As expected, ECs plated on VEGFR2^{R1032Q}-dECM showed a discontinuous and disorganized γ-actin pattern, coupled with disrupted VE-cadherin organization, as shown in Fig. 3C. To determine whether these structural alterations were accompanied by measurable changes in cellular mechanical properties, we performed label free, live-cell Brillouin microscopy 24 h after EC seeding. Compared with ECs cultured on standard gelatin-coated plates, cells seeded on VEGFR2^{WT}-dECM already displayed a significant increase in Brillouin frequency shift, indicating that exposure to tumor-derived ECM was sufficient to alter endothelial mechanical properties. Notably, this effect was further enhanced by VEGFR2^{R1032Q}-dECM, which induced a significantly higher Brillouin frequency shift compared with both control and VEGFR2^{WT}-dECM (Fig. 3D). These changes indicate altered intracellular mechanical properties, consistent with increased structural density and reduced compressibility [24]. Together with the increased mechanical tension across vinculin previously detected at FAs, these findings indicate that VEGFR2^{R1032Q}-dECM-induced cytoskeletal remodeling associates with measurable changes in endothelial mechanics.

Altogether, these data demonstrate that VEGFR2-driven ECM remodeling reprograms cytoskeletal architecture by promoting stress fiber formation, altering the mechanical properties, and disrupting cortical actin organization. These changes impair the mechanical integration between cell-matrix and cell-cell adhesions, priming ECs for junctional instability and vessel dysfunction.

2.4. Endothelial mechanical transition affects VE-cadherin junction stability and vessel permeability

The integrity of adherens junctions was analyzed to evaluate cell-cell cohesion and vessel functionality. ECs plated on VEGFR2^{WT}-dECM exhibited a linear and continuous VE-cadherin distribution along cell-cell contacts, consistent with stable and functional junctions. In contrast, ECs plated on VEGFR2^{R1032Q}-dECM, exhibited a discontinuous and fragmented VE-cadherin pattern, reflecting unstable and highly tensed junctions (Fig. 4A). Consistently, in these cells the disrupted VE-cadherin localization was closely associated with actin stress fibers, whereas in ECs plated on VEGFR2^{WT}-dECM, actin supported and stabilized intercellular junctions. VE-cadherin junction interface occupancy was quantified using the segmentation and analysis tool PolarityJam [23], as the ratio between the area of junctional proteins and the total cell-cell interface area, reflecting the junctional homogeneity. In ECs plated on VEGFR2^{WT}-dECM, higher occupancy values indicated more continuous and stable junctions, whereas in ECs plated on VEGFR2^{R1032Q}-dECM, junction coverage was reduced, consistent with a more fragmented and unstable VE-cadherin distribution (Fig. 4A). This observation was further corroborated by the gamma-actin/VE-cadherin co-staining (Fig. 4B). Consistent with these data, EC monolayers plated on VEGFR2^{R1032Q}-dECM displayed higher dextran permeability, supporting an alteration in endothelial barrier integrity (Fig. 4C).

According to recent evidence that connects the cell-cell junction integrity to tissue fluidity, defined as the transition from a solid-like state to a fluid-like state [25], we next analyzed the fluidity of EC monolayers seeded on dECMs. EC monolayers were monitored by time-lapse microscopy for 24 h. Although both culture conditions exhibited an initial physiological velocity drop, ECs plated on VEGFR2^{R1032Q}-dECM maintained a higher fluidity compared to ECs plated on VEGFR2^{WT}-dECM throughout the observation period (Fig. 4D–E). These results indicate that VEGFR2^{R1032Q}-dECM induced a mechanical reshaping of ECs, leading to altered adhesive properties, cytoskeletal rearrangements, and impaired adherens junctions. Consequently, disrupted cell-cell contacts impacted the collective behavior of the EC monolayer with potential critical implications for vessel formation, maturation, and function.

To validate these findings *in vivo*, VEGFR2^{R1032Q} Sk-MEL-31-derived tumors were stained for CD31 and VE-cadherin. Consistent with *in vitro* observations, VE-cadherin in VEGFR2^{R1032Q} Sk-Mel-31-derived tumors exhibited a discontinuous pattern reflecting junctional vessel instability, whereas VEGFR2^{WT} Sk-Mel-31 -derived tumors maintained linear, continuous junctions (Fig. 4F). Of note, a reduction of α-SMA covered vessels was highlighted in VEGFR2^{R1032Q} Sk-MEL-31-derived tumors (Fig. 4G and Supplementary Fig. 2). Together, these findings indicate that VEGFR2^{R1032Q}-associated ECM remodeling is linked to both endothelial junctional alterations and defective vascular maturation *in vivo*.

2.5. RhoA links cytoskeleton reorganization and vessel junctional stability

Given the central role of Rho GTPases in regulating actomyosin contractility and consequently junction stability [26], we investigated RhoA activation in ECs seeded on VEGFR2^{WT}- or VEGFR2^{R1032Q}-dECMs.

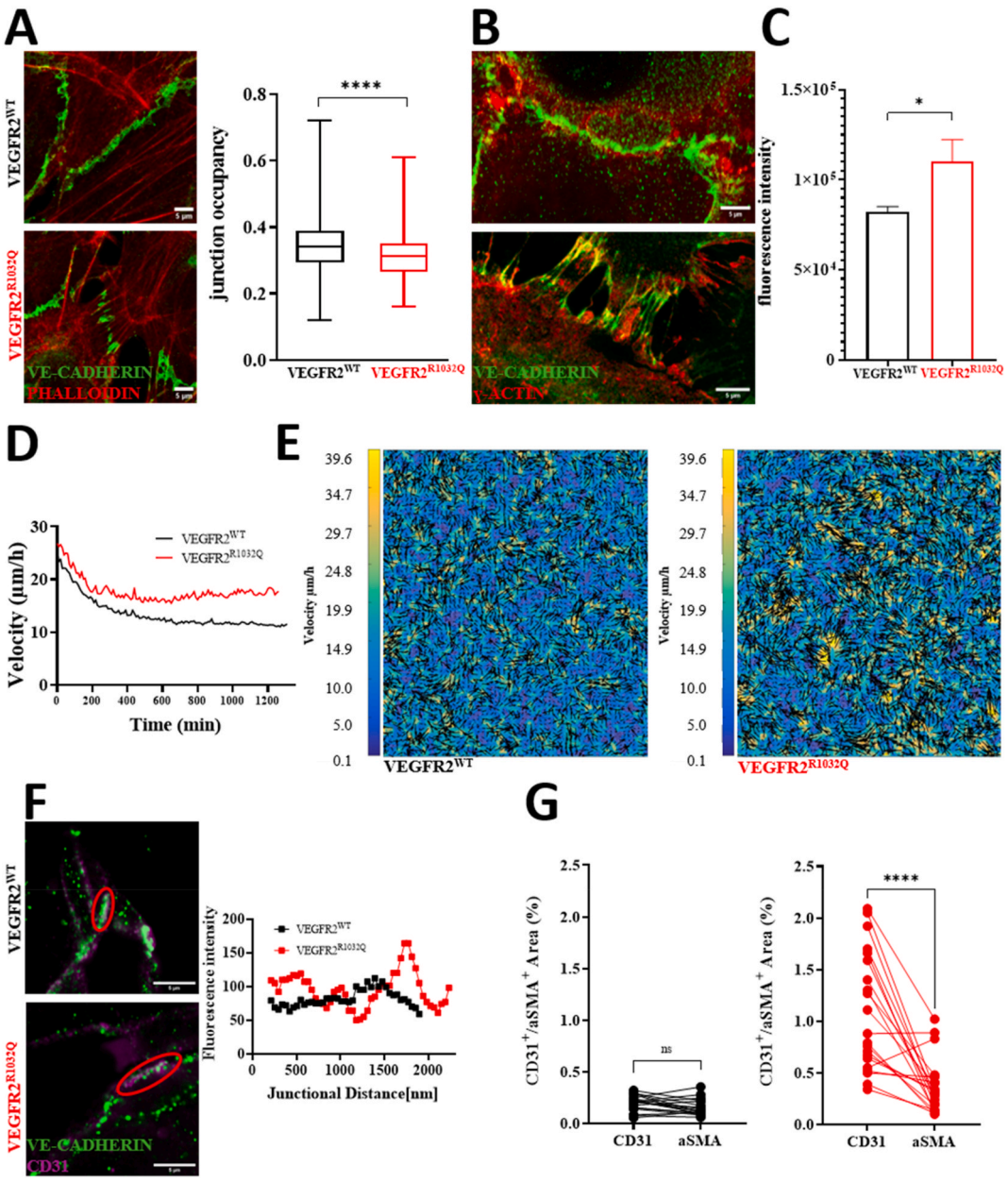


Fig. 4. Remodeled ECM impairs VE-cadherin junctions and EC monolayer fluidity. A) Representative images of phalloidin (red) and VE-cadherin (green) staining showing the interaction between cell-cell junctions and the actin cytoskeleton in ECs seeded on VEGFR2^{WT}- and VEGFR2^{R1032Q}-dECMs (left; scale bar 5 μm). Quantification of VE-cadherin junction occupancy is shown in the box plot (right). Single dots are not provided due to the high number of measurements derived from three independent experiments ****, $p < 0.001$, Student's t-test. **B)** Representative images showing the relationship between VE-cadherin (green) and cortical gamma-actin (red) (scale bar 5 μm). **C)** Endothelial monolayer permeability assessed by dextran assay in ECs seeded on VEGFR2^{WT}– or VEGFR2^{R1032Q}-dECMs. The graph shows dextran-associated raw fluorescence value. Data are presented as mean ± Standard Deviation (n = 4).*, $p < 0.05$, Student's t-test. **D)** Representative time course of the average monolayer fluidity for ECs on VEGFR2^{WT}- and VEGFR2^{R1032Q}-dECMs (respectively black and red line). Migration velocity was measured over 24 h (n = 3). **E)** Representative velocity heatmaps with overlaid vector fields showing the direction and magnitude of EC monolayer fluidity of ECs plated on VEGFR2^{WT}-dECM (left) and VEGFR2^{R1032Q} -dECM (right). (n = 3). **F)** Representative images of VE-cadherin (green) and CD31 (magenta) staining of tumors derived from VEGFR2^{R1032Q} Sk-Mel-31 and VEGFR2^{R1032Q} Sk-Mel-31 cells. The red circles indicate endothelial cell-cell junctions selected for fluorescence intensity profile analysis (scale bar 5 μm). The graph shows the VE-cadherin fluorescence intensity profile measured along the indicated junctional line. **G)** CD31/α-SMA correlation in tumors derived from VEGFR2^{WT}Sk-Mel-31 (left graph) and VEGFR2^{R1032Q} Sk-Mel-31 cells (right graph). Individual data are represented as dots (n = 15-20).****, $p < 0.001$, Student's t-test.

Both immunoprecipitation of the active GTP-bound RhoA and Rhotekin-pull down assay showed that ECs cultured on VEGFR2^{R1032Q}-dECM displayed an approximately two-fold increase in the fraction of active RhoA compared with cells cultured on VEGFR2^{WT}-dECM (Fig. 5A). Quantitative fluorescence analysis of active RhoA confirmed these data (Fig. 5B). In addition, a different RhoA distribution was highlighted. In ECs plated on VEGFR2^{WT}-dECM active RhoA localized predominantly at the plasma membrane, while in ECs cultured on VEGFR2^{R1032Q}-dECM, this spatial distribution was lost, suggesting both RhoA mis-localization and altered activation (Fig. 5B). In addition, in ECs plated on VEGFR2^{R1032Q}-dECM, phosphorylated myosin light chain (p-MLC) colocalized with basal actin stress fibers, consistent with enhanced actomyosin contractility (Fig. 5C). By treating ECs with the cell-permeable RhoA inhibitor CT04, we confirmed that

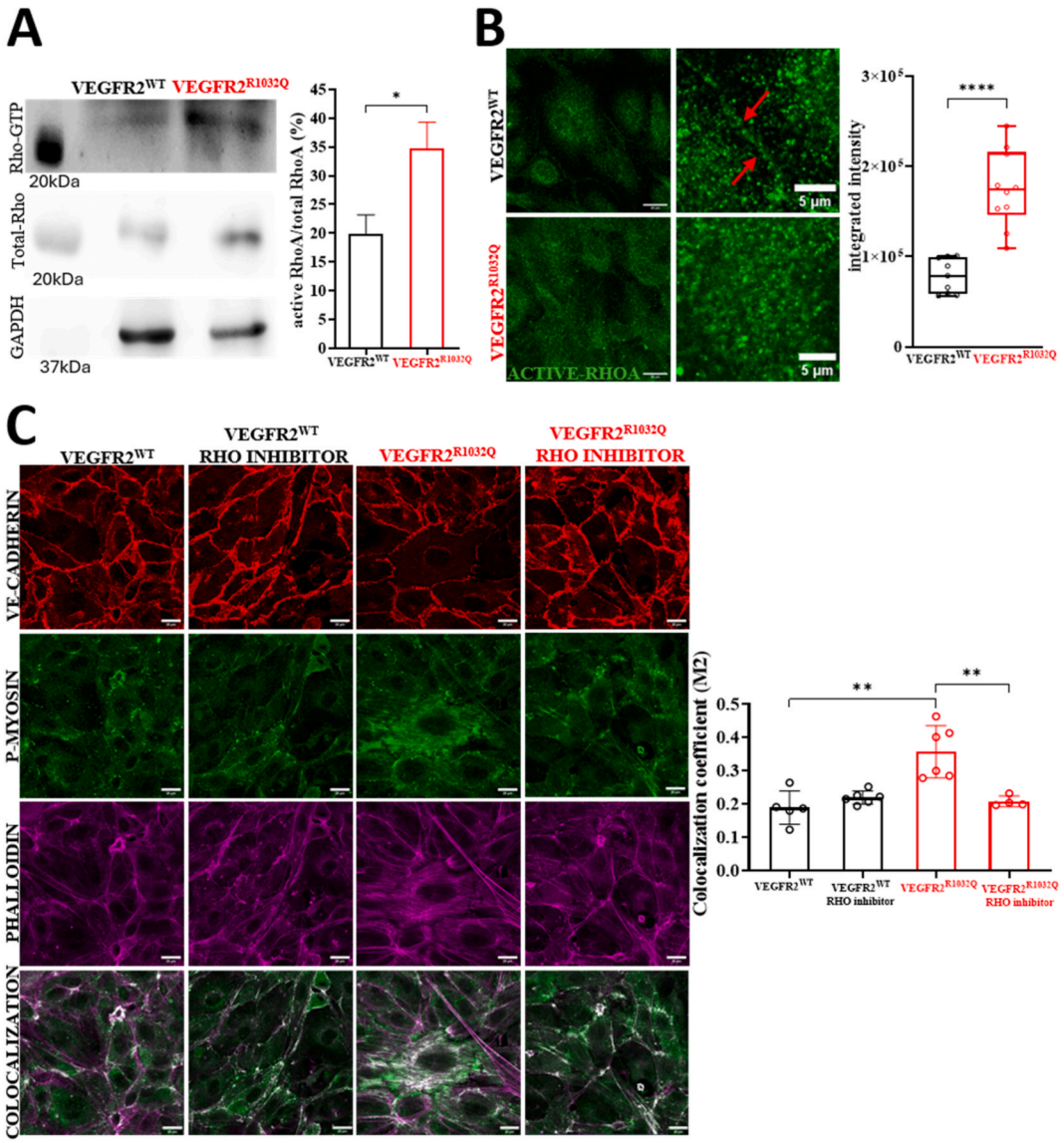


Fig. 5. RhoA mediates cytoskeleton reorganization in ECs. A) GTP-bound RhoA immunocomplexes recovered from ECs cultured on VEGFR2^{WT}- and VEGFR2^{R1032Q}-dECMs were probed with anti-total RhoA. 20 µg of total lysate were probed with anti RhoA (21 kDa) and anti-GAPDH (37 kDa). The bar graph on the right shows the active/total RhoA ratio. Data are shown as mean ± Standard Deviation (n = 2). *, $p < 0.05$, Student's t-test. **B)** Representative images of GTP-bound-RhoA immunofluorescence in ECs seeded on VEGFR2^{WT}- and VEGFR2^{R1032Q}-dECMs (left; scale bar 20 µm). Higher-magnification insets highlight RhoA membrane localization (right, scale bar 5 µm). Quantification of integrated intensity, normalized on cell area, is shown in the box plot. Individual data from three independent experiments are represented as empty dots ± Standard Deviation (n = 9-10). ****, $p < 0.001$, Student's t-test. **C)** Representative images of VE-cadherin (red), p-myosin light chain (p-MLC; green) and phalloidin (magenta) staining in ECs seeded on VEGFR2^{WT}- or VEGFR2^{R1032Q}-dECMs, untreated or treated with the cell-permeable Rho inhibitor CT04. Merged images show p-MLC/phalloidin colocalization (white) (scale bar 20 µm). The bar graph on the right shows the p-MLC/phalloidin Manders' colocalization coefficient (M2) for each experimental condition. Data are presented as mean ± Standard Deviation (n = 4-6). **, $p < 0.01$, Student's t-test.

cytoskeleton reorganization was RhoA dependent. Although CT04 had little effect on p-MLC/F-actin colocalization in ECs cultured on VEGFR2^{WT}-dECM, it significantly reduced p-MLC/F-actin colocalization in cells cultured on VEGFR2^{R1032Q}-dECM and decreased the abundance of basal stress fibers (Fig. 5C). Again, RhoA inhibition modified VE-cadherin distribution only in ECs cultured on VEGFR2^{R1032Q}-dECM. Qualitative analysis showed a more continuous and linear junctional pattern following CT04 treatment (Fig. 5C), suggesting a partial recovery of junctional organization. Together, these data indicate that the observed changes in endothelial mechanics coupled with cytoskeletal remodeling and junctional alterations induced by VEGFR2^{R1032Q}-dECM are, at least in part, dependent on altered RhoA activation and/or localization.

2.6. *Impaired mechanosensing affects EC response to flow-induced shear stress*

To investigate how VEGFR2^{R1032Q}-dECM affects endothelial cell mechanosensing, we examined multiple levels of the cellular response to mechanical stimuli. We first evaluated the primary cilium, a structural

component of the endothelial mechanosensory machinery. Primary cilia are microtubule-based structures that play a key role in endothelial homeostasis by acting as mechanosensors of intracellular and extracellular mechanical cues [27]. A significant reduction in ciliated cells was observed in ECs plated on VEGFR2^{R1032Q}-dECM compared to those on VEGFR2^{WT}-dECM (Fig. 6A), indicating that ECM remodeling affects components of the endothelial mechanosensory machinery. We next investigated whether these alterations were associated with impaired endothelial responses to haemodynamic forces. To this, ECs seeded on VEGFR2^{WT}- or VEGFR2^{R1032Q}-dECMs were subjected to a unidirectional laminar flow at 6 dyne/cm^2, using a microfluidic system. To assess the early mechanotransduction response to flow, we monitored intracellular Ca^{2+} dynamics (Supplementary video 1) [28]. As shown by the representative Ca^{2+} traces in Fig. 6B, flow onset induced a transient increase in cytoplasmic Ca^{2+} in both conditions, followed by a progressive decline after flow interruption. ECs cultured on VEGFR2^{R1032Q}-dECM exhibited a delayed Ca^{2+} response following flow onset and a more sustained Ca^{2+} signal after flow interruption compared with cells cultured on VEGFR2^{WT}-dECM. Following prolonged shear-stress exposure, ECs cultured on VEGFR2^{R1032Q}-dECM exhibited also a significantly higher nuclear-to-cytoplasmic YAP ratio compared with VEGFR2^{WT}--dECM (Fig. 6C), indicating enhanced nuclear YAP enrichment. These findings indicate that VEGFR2^{R1032Q}-dECM alters both early and downstream endothelial mechanotransduction response to flow. Alterations in flow-induced mechanotransduction were accompanied by morphological changes. Upon flow exposure, ECs plated on VEGFR2^{WT}-dECM elongated, polarized and aligned with the direction of flow. In contrast, ECs plated on VEGFR2^{R1032Q}-dECM exhibited impaired morphological adaptation to shear stress, with reduced elongation, polarization and flow alignment (Fig. 6D). In ECs plated on VEGFR2^{WT}-dECM, flow-induced polarization was associated with thinner cell-cell junctions and, consequently, lower interface occupancy than ECs plated on VEGFR2^{R1032Q}-dECM. In the latter condition, ECs retained a morphology resembling that observed under static conditions and displayed thicker, yet morphologically disorganized, junctions, consistent with our previous observations (Fig. 6E).

Supplementary data related to this article can be found online at https://doi.org/10.1016/j.canlet.2026.218848

Analysis of the actomyosin cytoskeleton further supported an altered morphological response to flow. Under flow, p-MLC lost its association with actin fibers observed under static conditions in both experimental conditions, displaying a perinuclear distribution. However, a reduced expression p-MLC at the cell periphery, along with a significant increase of p-MLC signal overlapping the nuclear area was observed in ECs cultured on VEGFR2^{R1032Q}-dECM compared to ECs plated on VEGFR2^{WT}-dECM (Fig. 6F). In parallel, actin filaments, segmented using the Cytospecter tool, were evaluated for their orientation by measuring circular variance, ranging from 0 (all vectors aligned) to 1 (vectors pointing in different directions). ECs plated on VEGFR2^{WT}-dECM, showed strong alignment of actin filaments along the direction of flow, supporting cellular polarization and morphological adaptation. Conversely, ECs plated on VEGFR2^{R1032Q}-dECM exhibited disorganized actin filaments accompanied by an altered distribution of FAs (Fig. 6G).

Finally, to assess functional consequences on cell dynamics, EC migration under flow was tracked over time (Supplementary video 2). Nuclei were tracked using the Fiji plugins StarDist and TrackMate, and nuclear velocity parallel to the flow was plotted over time. Initially, ECs plated on both dECMs migrated against the direction of flow, as indicated by negative velocity values (Fig. 6H). ECs plated on VEGFR2^{WT}-dECM reversed their migration direction within a few hours and migrated in the direction of flow, whereas ECs on VEGFR2^{R1032Q}-dECM became sensitive to flow forces only after 12 h, confirming delayed mechanosensitivity (Fig. 6H). Single cell trajectory analysis corroborated these results. During the first 12 h, ECs under both conditions migrated against the flow (red trajectories), for the following 12 h, ECs plated on VEGFR2^{WT}-dECM realigned with flow, while on VEGFR2^{R1032Q}-dECMs, EC migration persisted against the flow (Fig. 6I).

Supplementary data related to this article can be found online at https://doi.org/10.1016/j.canlet.2026.218848

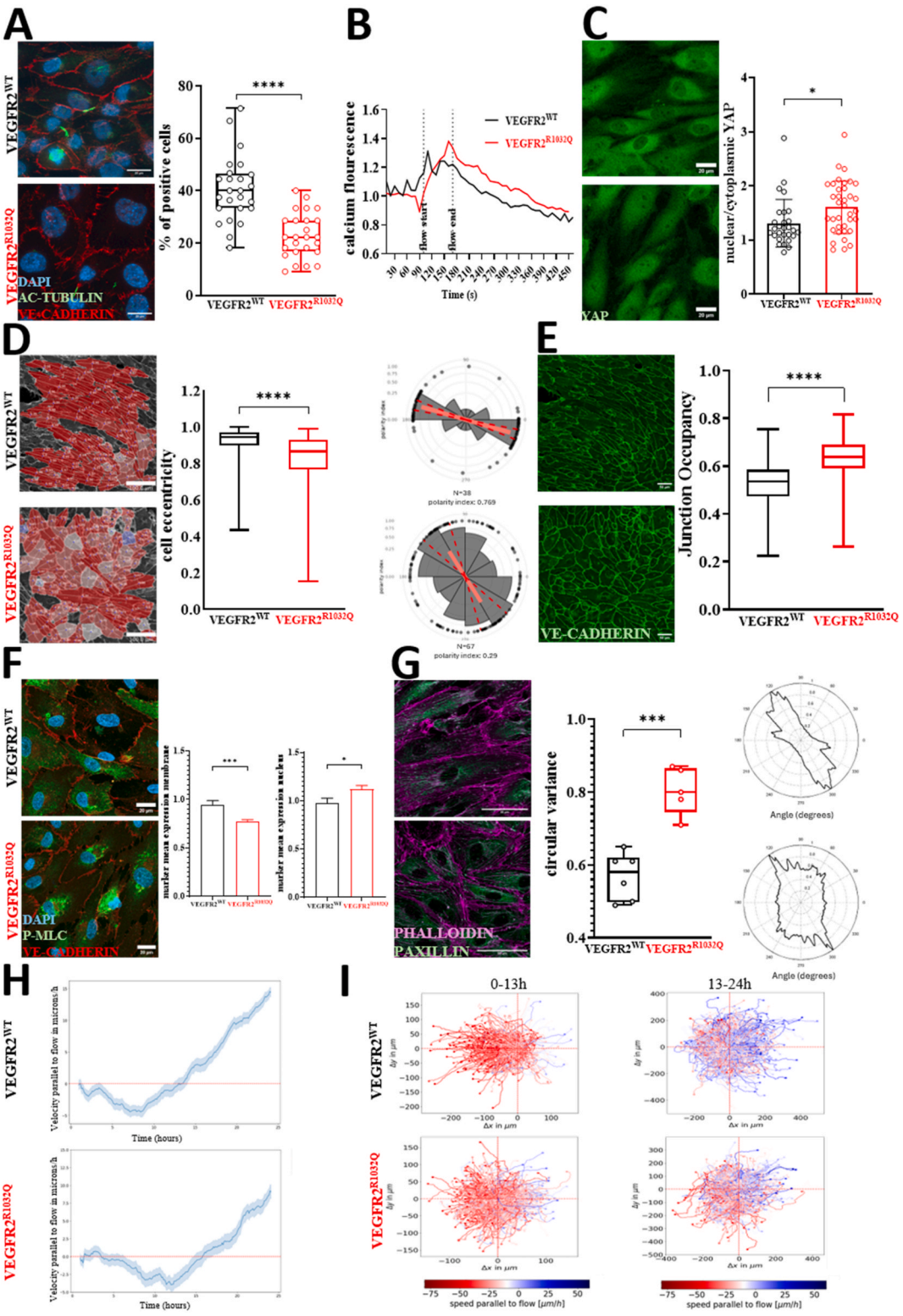
Collectively, these findings demonstrate that VEGFR2^{R1032Q}-dependent ECM remodeling interferes with multiple levels of EC response to shear stress, encompassing alterations in the mechanosensory machinery, early flow-induced mechanoresponses, and downstream mechanosensitive regulation. Impaired mechanotransduction was accompanied by defective morphological adaptation to flow, characterized by altered cell polarization, cytoskeletal and junctional remodeling, and directional migration. These results support a broader role for VEGFR2^{R1032Q}-dependent ECM remodeling in endothelial dysfunction and vascular instability.

3. Discussion

The tumor microenvironment (TME) is a dynamic system in which extracellular matrix (ECM) remodeling critically regulates tumor progression and vascular function. The ECM, which undergoes continuous changes in tumors, forms a 3D protein network which acts both as a structural scaffold and as a reservoir of signaling molecules and growth factors [3]. In this study, we show that oncogenic VEGFR2 signaling in tumor cells can drive ECM reprogramming that, in turn, impairs endothelial mechanosensing and compromises tumor vascular stability.

We previously demonstrated that aberrant VEGFR2 activation promotes tumorigenesis through an extensive remodeling of TME, including altered ECM organization and architecture in ovarian and melanoma models. Although the expression of VEGFR2 is detected in only approximately 30 % of melanoma cases and is therefore not a universal feature of the disease [29], the R1032Q substitution is the most frequently reported VEGFR2 mutation and has been identified predominantly in melanoma (cBioportal). Thus, our VEGFR2^{R1032Q}-expressing model represents a clinically relevant system for investigating the consequences of aberrant VEGFR2 signaling in this specific melanoma subset, particularly its ability to reprogram the ECM and thereby alter endothelial mechanosensing and vascular function. More specifically, aberrant VEGFR2 activation alters the expression of ECM components including fibrillar collagen COL1A2 and the FACIT collagen COL12A1, as well as ECM-modifying enzymes and soluble pro-angiogenic growth factors. Increased expression of several of these molecules has been associated with tumor aggressiveness and adverse clinical outcomes in patients with gastric and colorectal cancers [30–32]. Of note, tumor progression is, at least in part, driven by the composition and architecture of the ECM. Persistent ECM remodeling, can promote tissue stiffening and fibrosis [33,34] generating physical and biochemical conditions that support tumor cell proliferation, invasion and resistance to therapy while restricting immune-cell infiltration and modulating growth-factor availability [35,36]. These processes may be sustained by positive feedback mechanisms in which ECM proteases release fibrotic growth factors such as TGFB1, LTBP1, PDGFA, PDGFB, and BMPs, which in turn stimulate the synthesis of ECM components, particularly collagen chains [37,38]. COL1A2 and COL14A1 are highly expressed in fibrotic ECMs [39,40], and COL1A2 represents a TGF-β-responsive gene whose expression and deposition are upregulated across multiple cell types [32]. Notably, both TGF-β and VEGFR2 signaling pathways have been jointly implicated in extensive remodeling of the TME, and they are associated with adverse prognosis across multiple cancer types [41]. Accordingly, combined therapeutic strategies targeting these pathways have been explored to enhance immunotherapy efficacy and promote normalization of the tumor architecture [42].

According to previous evidence [43,44], ECM remodeling includes the altered expression of glycoproteins and proteoglycans such as TNC, TNXB, and VCAN, which may influence EC phenotype and function. The transcriptional and functional changes observed in ECs exposed to VEGFR2^{R1032Q} -dECM are therefore unlikely to reflect the effect of a



(caption on next page)

Fig. 6. Impaired mechanosensing affects EC behavior under flow conditions. A) Representative images of primary cilia positive ECs (left) plated VEGFR2^{WT}- and VEGFR2^{R1032Q}-dECMs. Acetylated tubulin stained primary cilia (green), scale bar 20μm. % ciliated ECs is shown in the box plot (n = 24 from two independent experiments) ****, p < 0.001, Student's t-test. **B)** Representative track of Ca^{2+} dynamics over time in ECs seeded on VEGFR2^{WT}- and VEGFR2^{R1032Q}-dECMs and subjected to flow. Cytoplasmic Ca^{2+} levels were monitored using the calcium indicator Fluo-4 AM. Dashed lines indicate flow onset and interruption. **C)** Representative images of YAP localization in ECs seeded on VEGFR2^{WT}- and VEGFR2^{R1032Q}-dECMs following exposure to unidirectional laminar flow at 6 dyne/cm^2 for 24 h. The bar graph shows the nuclear/cytoplasmic YAP ratio (n = 36 from two independent experiments). Data are presented as mean ± Standard Deviation.*, p < 0.05, Student's t-test. **D)** Representative color-coded map of cellular eccentricity measures ECs elongation after 24 h of unidirectional laminar flow (6 dyne/cm^2). Data represent three independent experiments. The quantification is shown in the box plot. Circular histograms show the distribution of cell orientations of a single image; the red arrow indicates the mean direction of the cell collective and its length is the polarity index. The red dashed lines indicate the 95 % confidence intervals. Black dots indicate single-cell measurements. The grey arrow indicates the polar vector that points in the direction of flow, and the length of the black bar indicates the signed polarity index (V). The polarity index ranges from 0 (not aligned with flow) to 1 (aligned with flow). Polarity index values displayed in circular graphs are 0.769 for ECs on VEGFR2^{WT}-dECM and 0.29 for ECs on VEGFR2^{R1032Q}-dECM. (n = 38-67 from three independent experiments)****, p < 0.001, Student's t-test. **E)** Junction occupancy of ECs on VEGFR2^{WT}- and VEGFR2^{R1032Q}-dECMs subjected to laminar flow at 6 dyne/cm^2 for 24 h measured with Polarityjam (scale bar 50 μm). Measurement shown in the box plot. Data represents three independent experiments, ****, p < 0.001, Student's t-test. **F)** Representative images of p-MLC (green), VE-cadherin (red) and nuclei (DAPI; blue) in ECs seeded on VEGFR2^{WT}- and VEGFR2^{R1032Q}-dECMs following exposure to unidirectional laminar flow at 6 dyne/cm^2 for 24 h. Quantification of p-MLC signals associated with the peripheral and nuclear regions is shown in the graphs on the right. Data are presented as mean ± Standard Deviation of two independent experiments (n = 66-70. *, p < 0.05, ***, p < 0.005, Student's t-test. **G)** Paxillin (green) and phalloidin (magenta) staining used to display the actin fibers orientation in ECs on VEGFR2^{WT}- and VEGFR2^{R1032Q}-dECMs, subjected to unidirectional laminar flow at 6 dyne/cm^2 for 24 h (scale bar 50 μm). Measured circular variance shown in the box plot represents the fiber alignment. The distribution of vectors representing the actin fibers direction is shown in the polar plots. ***, p < 0.005, Student's t-test. **H)** Velocity plot of EC migration under flow represents the velocity values relative to the time course of the acquisition. Negative values represent a velocity against the flow direction; positive values indicate a velocity which follows the flow direction. **I)** Single cell tracking of EC migration under flow. Color-coded single cell trajectories represent the distance of cell migration and the velocity relative to the flow direction. Cell trajectories were evaluated between 0 and 13 h of migration (left column) and between 13 and 24 h of migration (right column).

single matrix component. Rather, they appear to result from the combined effects of biochemical signals and altered matrix mechanics. In this context, TGF-β signaling and increased deposition of collagens and glycosaminoglycans may mutually reinforce ECM remodeling, establishing a matrix environment permissive for the acquisition of an early or partial EndMT-associated phenotype.

Our findings support a hierarchical model in which VEGFR2-dependent ECM remodeling disrupts the mechanical coordination between cell-matrix and cell-cell adhesions. Integrin-based FAs and VE-cadherin junctions do not function independently but form an integrated mechanosensitive network coupled through the actomyosin cytoskeleton. Thus, forces transmitted through one adhesive compartment can therefore influence the organization and stability of the other [45].

RhoA/ROCK-dependent contractility provides a plausible mechanistic link between these adhesive alterations and endothelial barrier dysfunction. RhoA activation promotes myosin light-chain phosphorylation and the assembly of contractile actin bundles, thereby increasing the forces transmitted between FAs and VE-cadherin complexes. Consistently, MLC phosphorylation and actin stress fibers organization, together with cell-cell junction integrity, are key determinants of endothelial barrier function [46]. Although a basal level of actomyosin tension is required to maintain junctional integrity, excessive or spatially unbalanced contractility can destabilize adherens junctions and increase endothelial permeability [46–48]. This mechanical uncoupling, observed in ECs plated on VEGFR2^{R1032Q}-dECM, is mediated by RhoA-dependent cytoskeletal reorganization, characterized by the formation of actin stress fibers. Accordingly, the increased RhoA-GTP levels and association of p-MLC with FA-anchored stress fibers observed in ECs exposed to VEGFR2^{R1032Q}-dECM, are consistent with a redistribution of intracellular tension toward cell-matrix adhesions. This mechanical imbalance provides an explanation for the coexistence of stabilized FAs, discontinuous VE-cadherin junctions, increased monolayer permeability, and enhanced migratory behavior. The Brillouin microscopy data further indicate that exposure to VEGFR2^{R1032Q}-dECM alters the intracellular mechanical state of ECs [24]. These measurements support the concept that the remodeled ECM acts as an active determinant of EC mechanics rather than merely representing a structural consequence of tumor progression. Nevertheless, Brillouin light scattering (BLS) principle is used to probe the complex longitudinal modulus, which reflect in a change in the Brillouin shift. The Brillouin shift is sensitive to variations in sample elasticity: in biological samples, cytoskeleton dynamics and intracellular solid-liquid variations have been found to be the main components that control the Brillouin shift. The modulus probed by BLS is different by the commonly measured Young's modulus, nevertheless, there has been shown a correlation between the two, but it is empirical and sample dependent [49]. Complementary assessments of traction forces, FA turnover, and cortical tension will therefore be required to determine how the observed Brillouin changes relate to actomyosin contractility and whether a feedback loop develops between ECM organization and intracellular tension.

In this context, the absence of an organized actin network under the lateral membrane contributes to junctional instability and enhanced migratory behavior, collectively facilitating EndMT and barrier disruption [50]. To this, cell-cell contacts play a pivotal role in maintaining the endothelial monolayer integrity. Modulation of the mechanical load experienced by cell-cell contacts reshapes VE-cadherin junctions, which appear discontinuous when subjected to high tension forces [50,51].

The functional consequences of this altered endothelial mechanical state were reflected in changes of the *in vivo* vascular organization. Indeed, endothelial junctional instability, together with reduced perivascular cell coverage, is consistent with the formation of a less mature and structurally unstable tumor vasculature. This mechanically destabilized phenotype is also compatible with the acquisition of an early or partial EndMT program. Importantly, our findings do not demonstrate complete EndMT but suggests that VEGFR2^{R1032Q} ECM shifts ECs toward an intermediate state characterized by increased migratory potential, impaired morphogenesis, junctional instability, and the expression of EndMT-associated markers [52]. Partial EndMT states are increasingly recognized as biologically relevant because ECs can acquire mesenchymal and invasive properties, impairing response to flow-induced shear stress [53–55]. The ability of a tumor-cell-derived ECM to induce this phenotype highlights a non-cell-autonomous mechanism through which oncogenic VEGFR2 signaling may reprogram the vasculature. Here, we also showed that ECs with mesenchymal features display alterations in both early and downstream mechanical responses to flow. The intracellular Ca^{2+} dynamics, and the nuclear localization of YAP observed in these cells confirmed a concomitant dysregulation of downstream mechanosensitive signaling under flow. In particular, the persistence of nuclear YAP under flow may reflect an ECM-imposed mechanically activated state that interferes with the ability of ECs to appropriately adapt to hemodynamic forces. Actually, this particular process will be worth further investigation in future studies since, according to published data that appear to be in contrast with our findings, flow-induced YAP nuclear translocation is essential to maintain vessel

function and lumen integrity [56]. This apparent discrepancy suggests that the functional consequences of YAP nuclear localization depend on the broader mechanical and molecular context. Therefore, further studies will be required to dissect its specific contribution before establishing a direct relationship with the observed vascular dysfunction.

Alterations in the mechanotransduction machinery are subsequently coupled with morphological defections under flow, such reduced polarization end eccentricity, which further support reduced and delayed response to flow. These alterations may indeed represent the mechanistic link coupling dysfunctional endothelial mechanics and *in vivo* vascular defects, potentially contributing to reduced vessel maturation and impaired barrier integrity. These findings may also have translational implications. A destabilized vascular network can facilitate tumor cell intra- and extravasation. Moreover, endothelial plasticity and EndMT contribute to therapy resistance, with ECs acquiring traits that protect tumor cells from chemotherapy, anti-angiogenic therapy, and radiotherapy [57]. EndMT has also been proposed to contribute to the generation of cancer-associated fibroblasts, further supporting tumor progression and therapy evasion [57,58]. These observations provide a rationale for targeting VEGFR2-dependent ECM remodeling as a potential strategy to counteract vascular dysfunction and improve therapeutic response [59–61]. Pharmacological VEGFR2 inhibition has previously been shown to partially restore ECM organization in this model, indicating that ECM remodeling represents a reversible component of aberrant VEGFR2 signaling [11]. Thus, in tumors characterized by aberrant VEGFR2 activity in cancer cells, VEGFR2 inhibition may act not only through direct effects on tumor cells and the vasculature but also by modifying the biochemical and mechanical microenvironment to which ECs are exposed. Collectively, our data highlight how the expression of aberrant VEGFR2 in melanoma cells enhanced tumor growth by directly activating pro-oncogenic intracellular signaling [7], mechanically supporting cancer cells [11] and modulating the integrity and stability of intratumoral blood vessels. These findings underscore a mechanistic paradigm in which tumor cells exploit ECM remodeling and impaired mechanosensing to orchestrate vascular instability, tumor progression, and therapy resistance, revealing potential avenues for therapeutically targeting the mechanobiological crosstalk between tumor and vasculature.

4. Material and methods

Cell cultures. Human melanoma Sk-Mel-31 cells, provided by Memorial Sloan Kettering Cancer Center (MSK00005207), were grown in RPMI supplemented with 10 % fetal calf serum (FCS), 1 % non-essential amino acids (NEAA) and 1 % Pen/Strep. Sk-Mel-31 cells stably expressing VEGFR2^{WT}- and VEGFR2^{R1032Q} were generated as previously described [62]. Primary Human Umbilical Vein Endothelial cells (HUVECs) were isolated from umbilical cord and grown in M199 supplemented with 20 % FCS, 1 % penicillin/streptomycin, 0,05 mg/mL of Heparin sodium salt, and bovine brain extract.

Matrix Decellularization. Sk-Mel-31-VEGFR2^{WT} and Sk-Mel-31-VEGFR2^{R1032Q} cells were seeded at 3x10^5 cells/cm^2 in complete medium and grown for eight days on different culture supports depending of experimental setting (e.g. 24 wells, Ibidi 8 wells etc). Decellularized matrices, hereafter referred to as VEGFR2^{WT}-dECM and VEGFR2^{R1032Q}-dECM, respectively, were obtained by treating the cell monolayers three times for 15 min with 4 mM PBS/EDTA until complete cell removal [11]. One well for each protocol was stained with DAPI to verify the complete decellularization. Decellularization was followed by six washes with PBS to restore physiological ions balance before HUVECs seeding. The resulting dECMs were either used immediately or stored in PBS at 4 °C for a maximum of three days.

Proteomic analysis. Decellularized matrices were harvested in 600 µL of RIPA buffer (0,5 M Tris-HCl pH 7,4, 1,5 M NaCl, 2,5 % deoxycholic acid, 10 % NP-40, 10 mM EDTA), yielding a protein concentration between 150 and 250 µg per sample. VEGFR2^{WT}- and VEGFR2^{R1032Q}-dECMs were dissolved directly in EasyPep lysis buffer. 100 µg of each sample were processed using the EasyPep MS Sample Prep Kit (Thermo Fisher Scientific, Waltham, Massachusetts, USA) following manufactured instructions. After reduction and alkylation, proteins were digested with trypsin/LysC. Following purification, peptides were quantified using the Pierce Quantitative Colorimetric Peptide Assay kit (#23275, Thermo Fisher Scientific). A total of 1.9 µg of each sample was injected into an UltiMate 3000 RSLC nanosystem coupled to an Orbitrap Exploris 240 mass spectrometer (Thermo Fisher Scientific). Peptide were separated on Easy-Spray Pepmap RSLC18 column (2 µm, 75 cm × 75 µm) at a flow rate of 200 nL/min using a gradient of solvent B (80 % acetonitrile/0.1 % formic acid, solvent A: 0.1 % formic acid in water) from 2 % to 40 % over 200 min. Solvent B was then increased to 99 % over 20 min and maintained at 99 % for 10 min, after which the column was re-equilibrated for 15 min. Data was acquired in positive ion mode using a data-dependent acquisition strategy. The MS1 *m/z* range was set to 375-1500 at a resolution of 120,000 (at *m/z* 200), with an AGC target of 3x10^6 and automatic injection time. MS2 acquisition was switched when ion intensity exceeded 1x10^4, using an automatically determined *m/z* range, a normalized HCD collision energy of 30 %, an AGC target of 7.5x10^4, and a maximum injection time of 40 ms. MS2 resolution was set to 15,000 at m/z 200. The internal calibrant was employed in run-start mode. Five technical replicates were analyzed for each biological sample. Raw data generated using Xcalibur 4.2 software (Thermo Fisher Scientific) were analyzed with Proteome Discoverer 2.5 (Thermo Fisher Scientific) using the SEQUEST algorithm. The carbamidomethylation of cysteines was considered a fixed modification, whereas phosphorylation of serine, threonine, and tyrosine was considered a variable modification. Oxidation (M) and deamidation (N, Q) were also included as variable modification. The false discovery rate (FDR) was evaluated using a target-decoy strategy. The strict FDR was set as 0.01 and the relaxed FDR to 0.05. Differentially expressed proteins were filtered according to their extracellular localization using the ShinyGO 0.85 bioinformatic enrichment tool. Contaminants were removed. Differentially expressed master proteins were then selected using thresholds of log 2 fold change (FC) ≥ 0.3 and $p < 0.05$. Fold changes, adjusted p values, and accession numbers were used for pathway analysis using iPathwayGuide software (Advaita Corporation, Ann Arbor, Michigan, USA) based on Advaita's proprietary impact analysis method.

In vivo tumorigenesis. In vivo tumorigenesis were approved by Italian "Ministero della Salute" (authorization no. 266/2016-PR) and performed in accordance with national and European guidelines and regulations. Mice were obtained from Envigo (Italy) and housed at the Mouse Facility of the Department of Molecular and Translational Medicine of the University of Brescia. Mice were maintained in ventilated cage racks at 22-24 °C, under a 12 h/12 h light/dark cycle, with ad libitum access to food and water for 40 days. NOD/Scid mice were injected subcutaneously (s.c.) into the dorsolateral flank with 4x10^6 Sk-Mel-31-VEGFR2^{WT} or Sk-Mel-31-VEGFR2^{R1032Q} cells suspended in 100 µL of a 1:1 PBS/Cultrex reduced growth factor. Tumors were harvested and processed for histological analysis.

Histological staining. Formalin-fixed, paraffin-embedded (FFPE) tissue sections were stained with CD31 (#DIA-310, Dianova, Eching, Germany), VE-Cadherin (#ab33168, ABCAM, Cambridge, UK), vimentin (#V5255, Sigma-Aldrich, St. Louis, Missouri, USA), and α-SMA (#MA1-06110, Thermo Fisher Scientific). Primary antibodies were detected using appropriate Alexa Fluor 488- or Alexa Fluor 594-conjugated secondary antibodies (Molecular Probes). Nuclei were stained with 4',6-diamidino-2-phenylindole (DAPI, Sigma-Aldrich) or TO-PRO-3 (#T3605, Thermo Fisher Scientific). Samples were analyzed using a confocal LSM880 two-photon microscope (Carl Zeiss S.P.A, Oberkochen, Germany) equipped with Plan-Neofluar 20X/0.5 NA and 40X/0,75 objective (Carl Zeiss S.P.A.). For Second Harmonic Generation (SHG) imaging, collagen bundles were visualized using a Chameleon IR Laser

Table 1
Primer sequences used for quantitative PCR.

Gene	Forward	Reverse
Hs_Ve-Cad	ACAACGAGGGCATCATCAA	GGTAGAAAGGCTGCTGGAAA
Hs_ZO1	CCTTCCACCTCTTACTCACCA	GGTTCTGCCTCATCATTTCC
Hs_VCAM	GCGGAGACAGGAGACACAG	GCAAAATAGAGCACGAGAAG
Hs_Vimentin	CGCCAGATGCGTGAAATG	ACCAGAGGGAGTGAATCCAGA
Hs_SNAIL1	AATCGGAAGCCTAACTACAGCG	GTCCCAGATGAGCATTGGCA
Hs_SNAIL2	TGACCTGTCTGCAAATGCTC	CAGACCCTGGTTGCTTCAA
Hs_S100A4	CCTGGATGTGATGGTGTCC	TCGTTGTCCCTGTTGCTGT
Hs_ITGB3	CATCACCATCCACGACCGAA	GGTTGTTGGCTGTGTCCCAT
Hs_ITGAV	TATGCCATCACCGTTGAAAT	TATGCCATCACCGTTGAAAT
Hs_ITGA1	CCGAAGAGGTACTTGTTGCAGC	CCGAAGAGGTACTTGTTGCAGC
Hs_ITGA2	CCGAAGAGGTACTTGTTGCAGC	CCACAGAGGACCACATGTGAGAAAA
Hs_ITGB1	GGATTCTCCAGAAGGTGGTTTCG	TGCCACCAAGTTTCCCATCTCC

(Ex $\lambda = 860$, Em $\lambda = 430/10$). Images were analyzed using ImageJ software.

Scratch assay. 4×10^5 HUVECs/well were seeded on Sk-Mel-31 VEGFR2^{WT}- and VEGFR2^{R1032Q}-dECMs. EC monolayers were scratched using a 200 μL pipette tip and incubated in growth medium. Cell monolayers were photographed after scratch (T0) and after 16 h (T16). The area covered by migrating cells was quantified using ImageJ software (National Institutes of Health, Bethesda, Maryland, USA). Results were expressed as Area $_{T16}$ -Area $_{T0}$

Haptotaxis in Boyden's Chamber. Sk-Mel-31-VEGFR2^{WT} and Sk-Mel-31-VEGFR2^{R1032Q} cells were seeded and maintained for 8 days on the lower portion of PVP-free polycarbonate filters (8 μm pore size, Costar, Cambridge, USA) to prepare dECMs. After decellularization, PVP-free filters were inserted in a Boyden chamber. 50 μL of HUVECs (2.5x10^6/mL cells in M199 5 % FBS) were seeded in the upper compartments of a Boyden's chamber. The lower compartments were filled with 10 % FBS-M199. As a negative control 1 % FBS-M199 was used.

After 5 h of incubation at 37 C°, cells migrated to the lower side of the filter were stained with Diff-Quik (Dade-Behring, Deerfield, Illinois, USA) and counted. Five random selected fields were analyzed for each sample, with experiments performed in triplicate.

Gene expression. Total RNA was extracted using TRIzol Reagent (Thermo Fisher Scientific) according to the manufacturer's instructions. Complementary DNA (cDNA) was made from 2 μg of total RNA using MML-V (Thermo Fisher Scientific). Real-time PCR was performed using ViiA7 Real-Time PCR System (Thermo Fisher Scientific), and data was analyzed with ViiA7 Real-Time Software (Thermo Fisher Scientific). Primer sequences used in this work are listed in Table 1.

FLIM/FRET analysis of Vinculin tension sensor. HUVECs were transiently transfected to express Vinculin Tension Sensor (VinTS) or its Tail-Less control (VinTL) [63]. At 24 h after transfection, cells expressing VinTS and VinTL were seeded on VEGFR2^{R1032Q}- and VEGFR2^{WT}--dECMs in μ-slide (IBIDI, Grafilfing, Germany). Cells expressing Vinculin-mTFP1 were used to determine donor alone fluorescence lifetime. The fluorescence lifetime of mTFP1 fluorophore, in presence or absence of the acceptor fluorophore, was evaluated in all experimental conditions with an LSM880 confocal two-photon microscope equipped with a time-correlated single-photon counting (TCSPC) module (PicoQuant, Berlin, Germany). The donor was excited at 860 nm using a Chameleon Vision II picosecond-pulsed laser operating at a repetition rate of 80 MHz (Coherent Inc, Santa Clara, California, USA). TCSPC decay curves were fitted using a single-exponential decay model employing the SymphoTime 64 software (PicoQuant). For each individual cell, focal adhesion areas were selected as regions of interest (ROIs), and the average lifetime within each ROI was determined. FRET efficiency (E) was calculated using the following equation where τ_D and τ_{DA} are the lifetime values of donor fluorophore in the absence and presence of the acceptor, respectively.

$$E = 1 - (\tau_{DA}/\tau_D)$$

FRET analysis of FAT-FAK sensor. To analyze the FAK activity, ECFP/FRET emission ratio was analyzed in HUVECs transfected with FAT-FAK FRET biosensor (Addgene, Watertown, Massachusetts, USA) [19]. The FAT-FAK FRET sensor contains the ECFP/YPet FRET pair interspaced by a flexible linker and a FAK substrate sequence and the FAT domain for FA localization. Transfected cells were seeded onto VEGFR2^{WT}-dECM or VEGFR2^{R1032Q}-dECM for 24 h. Images of ECFP and FRET channels were obtained exciting the biosensor at 458 nm and acquiring emissions at 515 ± 50 nm and 570 ± 50 nm, respectively using a LSM880 laser-scanning microscope (Carl Zeiss S.P.A) equipped with a Plan-Apochromatic 63X/1,4 Oil DIC objective (Carl Zeiss S.P.A). Images were then analyzed with the Imagej software to measure the ECFP/FRET ratio as a read out of FAK activity in FAs. At least 15 images for experimental conditions were analyzed in each of three independent experiments.

Brillouin microscopy. HUVECs (2x10^5) were seeded onto 35-mm glass dishes (IBIDI, Grafilfing, Germany) coated with porcine gelatin (#G2500, Sigma-Aldrich) (1 % in ultrapure distilled water), VEGFR2^{WT}-dECM or VEGFR2^{R1032Q}-dECM, and analyzed after 24 h. Brillouin frequency shifts were measured using an Olympus IX-81 microscope with a Discoverer™ Brillouin system (CellSense GmbH, Berlin, Germany) equipped with a dual-crossed virtually imaged phased array (VIPA) configuration and a 780 nm excitation laser. Brillouin measurements were acquired with a 40x/NA = 0.75 Oil objective (Olympus, Tokyo, Japan), at a step size of 2 μm in a 37 °C temperature-controlled stage (Ibidi, Germany). Brillouin shifts measurements were obtained using BMicro (https://github.com/BrillouinMicroscopy/BMicro). For each sample, the mean Brillouin shift was calculated from the acquired pixel-wise measurements and subsequently plotted using GraphPad Prism. Measurements were performed in four independent experiments.

Monolayer fluidity. Endothelial monolayer fluidity was assessed by time-lapse video microscopy. 6x10^5 HUVECs were seeded overnight in a 6-well plate containing VEGFR2^{WT}-dECM or VEGFR2^{R1032Q}-dECMs. Cells were imaged using an Axio Observer microscope (Carl Zeiss) equipped with a Plan-Neofluar 20X/0.5 NA objective, and phase-contrast images were acquired every 10 min for 1440 min. A constant temperature of 37 °C and 5 % CO_2 were maintained throughout the experiment using a heated stage and environmental chamber. The videos obtained were analyzed using particle image velocimetry (PIV) using the PIVlab analysis tool in MATLAB (http://www.PIVlab.de) [64]. Velocity vector fields were calculated for each frame using a two-pass interrogation procedure, with interrogation windows of 100x100 pixels in the first pass and 50x50 pixels in the second pass. Mean values and standard deviation were determined from six replicates in two independent experiments.

Immunofluorescence analysis. 1x10^5 HUVECs were seeded on dECM in Ibidi 8 well chamber for 24 h. Where indicated, cells were treated with 1 μg/mL of Rho inhibitor CT04 (Cytoskeleton, Denver, Colorado, USA) for 180 min. Cells were then fixed with 4 % PFA, permeabilized with 0.1 % Triton-X100 and immunostained with antibodies against Paxillin (#05-417, Sigma-Aldrich), VE-Cadherin (#ab33168, ABCAM, Cambridge, UK), ɣ-actin (#MABT824, Sigma-Aldrich), phospho-Myosin (#3671, Cell signaling), Rho-GTP (#26904, New East Biosciences, King of Prussia, Pennsylvania, USA), YAP (#sc-101199, Santa Cruz, Dallas, Texas, USA) or acetylated tubulin (#T6793, Sigma-Aldrich). Where indicated, F-actin and nuclei were visualized using fluorescently labelled phalloidin, and 4',6-diamidino-2-phenylindole (DAPI, Sigma-Aldrich), respectively. Primary antibodies were detected using appropriate AlexaFluor 488- or AlexaFluor 594-conjugated secondary antibodies (Molecular Probes). Images were acquired using a LSM880 confocal microscope (Carl Zeiss) and analyzed using ImageJ software or Zen black 2.3 software (Carl Zeiss). For Rho-GTP fluorescence intensity measurement, images were analyzed using a fixed threshold value of 25 by ImageJ tool. Fluorescence intensity was normalized to the cell area. Focal adhesions were quantified from paxillin-stained images using ImageJ. Data were expressed as the number of focal adhesions per cell. The phospho-myosin/phalloidin colocalization was analyzed employing the colocalization tool implemented in Zen black 2.3 software. Four optical sections were acquired for each field, and maximum intensity projections of the resulting z-stack were generated before analysis. The Manders' Colocalization Coefficient (M_2) was calculated as:

$$M_2 = \sum_i C2_{i,\ colocal} / C2_i$$

Primary cilia length was measured from acetylated tubulin-stained images using Zen black 2.3 software. Unless otherwise indicated, experiments were performed at least three independent times, with 10-15 images analyzed per experimental condition.

Rho-GTP Immunoprecipitation. HUVECs (2x10^6) were seeded on VEGFR2^{WT}- or VEGFR2^{R1032Q}-dECMs-coated 10 cm dishes for 24 h. Cells were lysed on ice in 600 μL of lysis buffer (50 mM Tris pH 7.5, 10 mM $MgCl_2$, 0.3 M NaCl, 1 % NP40, protease and phosphatase inhibitors, Merck KGaA, Darmstadt, Germania). Lysates were centrifuged at 13,000 x g for 15 min to remove insoluble debris, and protein concentration was quantified for normalization. For each experimental condition, 1.8 mg of total protein lysates were incubated for 30 min at 4 °C under rotation with 4 μg of anti-Rho-GTP antibody and 40 μL of anti-mouse IgG-Agarose beads (#A6531, Sigma-Aldrich) pre-equilibrated in lysis buffer. Agarose beads were recovered by centrifugation at 2000 x g for 1 min, washed three times with 500 μL of wash buffer (25 mM Tris pH 7.5, 30 mM $MgCl_2$, 40 mM NaCl) and, resuspended in 30 μL of SDS sample buffer. Samples were separated by 15 % SDS-Page, and membranes probed with an anti-total-Rho antibody (#sc-418, Santa Cruz). An aliquot of total cell lysates (20 μg) was analyzed in parallel with anti-total-Rho and anti-GAPDH (#sc-365062, Santa Cruz) antibodies to assess total Rho levels and protein loading, respectively. Chemiluminescent signals were acquired using a ChemiDoc™ Imaging System (BioRad, Hercules, California, USA). To avoid interference from immunoglobulin light (~25 kDa) and heavy (~50 kDa) chains, the membrane containing immunoprecipitated Rho-GTP was cut below 25 kDa before imaging. Densitometric analysis was performed using ImageJ software. As an independent approach to assess active Rho, the Rho-GTP pull-down assay was also performed using Rhotekin-RBD beads (Cytoskeleton) for incubation with cell lysates.

Macromolecular permeability. HUVECs seeded at a density of 3x10^5 cells per well onto 24-well cell culture inserts (8.0 μm, Corning, New York, USA) containing VEGFR2^{WT}- or VEGFR2^{R1032Q}-dECM for 24 h to allow the formation of a confluent monolayer. Rhodamine-conjugated dextran (70 kDa, Sigma-Aldrich) was then added to the upper chamber. Molecular permeability across the HUVEC monolayer was assessed after 90 min by measuring the fluorescent signal in the lower chamber using a fluorescent plate reader (EnSight, PerkinElmer, Waltham, MA, USA).

Expansion microscopy. Cells were fixed with 4 % PFA for 10 min at room temperature (RT) and treated with 0.1 M glycine for 10 min. After three washes with PBS, samples were incubated in Blocking buffer (PBS, 0.1 % Tween-20, 1 % BSA, 5 % goat serum) for 30 min followed by overnight incubation at RT with 0.5 μM Actin ExM Range (#PL-3-04 range, Chrometra, Kortenaken, Belgium), and 20 μg/mL DAPI (#D9542, Sigma-Aldrich) diluted in blocking buffer. Samples were washed twice with PBS-T, and incubated with 0.1 mg/mL Acryloyl-X SE (6-acryloyl-amino-hexanoic acid, succinimidyl ester, AcX; Invitrogen) in PBS overnight at 4 °C. Samples were washed twice with PBS for 15 min, added with Gelation solution 40 % (v/v) 49:1 Acrylamide:Bis-acrylamide solution (Sigma-Aldrich), (5 M NaCl, 33 % sodium acrylate, 0.2 g/mL APS, and 0.2 g/mL TEMED in PBS) for 5 min on ice. Samples were incubated for 1 h at 37 °C to allow gel polymerization. Samples, digested overnight at RT with 0.2 mg/mL (8 U/mL) Proteinase K (#EO0491, Thermo Fisher Scientific) in Digestion buffer (25 mM EDTA, 50 mM Tris-HCl pH 8.0, 0.5 % Triton X-100, 1 M NaCl). Samples were expanded approximately fourfold in deionized water. Expanded samples were imaged using a Zeiss LSM880 laser-scanning microscope, equipped with Plan-Apochromatic 63X/1,4 Oil DIC objective and Airyscan. Images were analyzed using ZEN software (Carl Zeiss) and ImageJ. Fifteen images from different cells were analyzed for each experimental condition. Experiments were performed at least twice independently. To segment and measure the area of basal actin corrals, images were analyzed using ImageJ software. Briefly, images were converted to 8-bit and segmented using Otsu thresholding with a dark background The resulting binary masks were eroded twice, inverted and processed using the watershed algorithm to separate adjacent structures. Individual corrals were identified using the Analyze Particles function, excluding objects intersecting the image boundaries. The segmented masks were overlaid on the original images, and the area of each corral was measured. Corrals with an area <0.001 μm^2 or >1.0 μm^2 were excluded from the analysis to minimize artifacts arising from local image-resolution limitations.

Lateral cortical actin thickness was quantified using ZEN Blue software by drawing a line perpendicular to the plasma membrane across the entire width of the actin-positive cortical layer. Measurements expressed in μm were performed at 3 independent positions per cell and averaged to obtain a single value for each cell. The measurement was repeated for at least fifteen images across three independent experiments.

***In vitro* flow-induced shear stress.** 3x10^5 HUVECs were cultured to confluence onto IbiTreat μ-Slide I Luer chambers (0.4 mm channel height; Ibidi) containing VEGFR2^{WT}- or VEGFR2^{R1032Q}-dECMs in degassed EGM2 medium (Lonza, Basel, Switzerland). Unidirectional laminar flow corresponding to a shear stress of 6 dyn/cm^2 was applied for 24 h at 37 °C in a CO_2 incubator using a Ibidi Pump System equipped with a red perfusion set (15 cm tubing length, 1.6 mm inner diameter, 10 mL reservoirs). The following pump parameters were used: calibration factor, 0.99; medium viscosity, 0.0072 dyn*s/cm^2; pressure, 8.4 mbar; flow rate, 6.30 mL/min; and flow-switching time, 22s. Static control cells were maintained under otherwise identical culture conditions for the same duration. After 24 h, cells were fixed in 4 % PFA and stained with the previously described antibodies. Images were acquired using an LSM980 laser-scanning microscope (Carl Zeiss) equipped with a Plan-Neofluar 20X/0.5 NA objective as 3× 3 tiled fields. For cell segmentation using Cellpose. Nuclei (DAPI) and membrane (VE-cadherin) channels were used as references. When necessary, segmentation masks were manually corrected before subsequent analysis. The resulting masks were analyzed using PolarityJam bioinformatic tool [65] to quantify cell polarity, elongation, cell area, and junctional interface

occupancy. For each experimental condition, 10 fields were analyzed, corresponding to approximately 150 cells/field. Truncated or isolated cells were excluded during segmentation or automatically by PolarityJam when below the detection threshold. Experiments were performed independently at least three times. Higher-magnification images acquired using a Plan-Apochromatic 63X/1,4 Oil DIC objective were analyzed for actin filament orientation using the Cytospectre bioinformatic tool [66]. For live-cell imaging under flow, nuclei were labelled with the live-cell nuclear dye SPY555-DNA (Stein am Rhein, Switzerland). Cells were exposed under unidirectional laminar flow at 6 dyn/cm^2, using a YELLOW/GREEN perfusion set (50 cm tubing length, 1.6 mm inner diameter, 10 mL reservoirs), and imaged using an LSM980 laser-scanning microscope (Carl Zeiss) equipped with a Plan-Neofluar 20X/0.5 NA objective. Images were acquired every 10 min for 1440 min under continuous flow. Live-cell images acquired as 3 x 3 tiled fields were segmented using Cellpose and analyzed with Polarityjam for cell polarity, elongation and junction interface occupancy as described above. Nuclear tracking was performed using the StarDist plugin in Fiji, and nuclear trajectories were analyzed using the TrackMate plugin. Cell velocity and trajectories were subsequently plotted using Jupiter Notebook within the Anaconda Navigator platform.

For Ca^{2+} intracellular dynamics, cells subjected to shear stress for 24h, were incubated for 10 min with 6 μM Fluo-4 AM (Thermo Fisher Scientific) in HBSS without Ca^{2+} and magnesium. Intracellular calcium dynamics were followed by time-lapse imaging using a Plan-Neofluar 20X/0.5 NA objective. Fluorescence baseline was recorded during the first 2 min (1 image every 10s) in the absence of shear stress. Laminar flow was then applied for 1 min Ca^{2+} dynamics was monitored for 7 min (1 image every 10 s) [28]. Image analysis was performed using ImageJ. Different ROIs were randomly selected. Five cells for each field were analyzed. Results were expressed as F (fluorescent intensity)/F_0 (mean baseline fluorescence). At least three randomly selected ROIs were analyzed in each of four independent fields per experimental condition. Experiments were performed twice independently.

Statistical analyses. Statistical analyses were performed using GraphPad Prism10 (GraphPad Software). Student's *t*-test for unpaired data (2-tailed) was used to test the probability of significant differences between two groups of samples. For more than two groups of samples, data were statistically analyzed with one-way ANOVA (analysis of variance), and individual group comparisons were evaluated by Bonferroni multiple comparison test. The significance level was set at $P < 0.05$.

CRediT authorship contribution statement

Mattia Domenichini: Writing – original draft, Validation, Supervision, Formal analysis, Conceptualization. **Michela Corsini:** Investigation, Funding acquisition, Formal analysis, Conceptualization. **Cosetta Ravelli:** Investigation, Formal analysis. **Anastasia Ricci:** Investigation. **Elisa Moreschi:** Investigation. **Elisabetta Grillo:** Investigation. **Camilla Maggi:** Investigation. **Gianluca Baldanzi:** Investigation, Writing – review & editing. **Sonia Chiodini:** Investigation. **Diana Eveline Sanchez-Amador:** Investigation. **Julia Kraxner:** Methodology, Investigation. **Michael G. Monaghan:** Investigation, Writing – review & editing. **Holger Gerhardt:** Methodology, Investigation. **Michele Menotta:** Investigation, Data curation. **Stefania Mitola:** Writing – review & editing, Writing – original draft, Supervision, Methodology, Investigation, Funding acquisition, Conceptualization.

Ethics declaration

This study was conducted in accordance with the following guidelines for animal welfare and/or reporting: Italian. This study was approved by the Italian "Ministero della Salute". (Approval No. 266/2016-PR)

Declaration of competing interest

The authors declare that they have no known competing financial interests or personal relationships that could have appeared to influence the work reported in this paper.The author is an Editorial Board Member/Editor-in-Chief/Associate Editor/Guest Editor for this journal and was not involved in the editorial review or the decision to publish this article.

Acknowledgments

This work was supported by grants from MIUR to Consorzio Interuniversitario Biotecnologie (CIB), by Associazione Italiana Ricerca sul Cancro AIRC (AIRC grant IG17276 to S.M.); AIRC fellowship for Italy (grant n° 26917 to M.C.); PNRR - CN3 "Sviluppo di Terapia Genica e Farmaci con Tecnologia ad RNA" PNRR M4C2-Investimento 1.4-CN00000041 finanziato dall'Unione Europea–Next GenerationEU"(to M.S., and M.C.); Cariplo Foundation to EG. Research funds from University of Brescia (ex 60 %) 2024 to S.M, E. G. and M.C., and "5 per mille" to M.C. Funding bodies did not have any role in designing the study, collecting, analyzing, and interpreting data or in writing the manuscript.

The authors performed experiments at the Imaging Platform, Cryogenic bank, and Animal facility of the Department of Translational and Molecular Medicine of the Università degli Studi di Brescia.

Appendix A. Supplementary data

Supplementary data to this article can be found online at https://doi.org/10.1016/j.canlet.2026.218848.

References

[1] N.M. Anderson, M.C. Simon, The tumor microenvironment, Curr. Biol. 30 (16) (2020) R921–R925, https://doi.org/10.1016/j.cub.2020.06.081.
[2] K.E. de Visser, J.A. Joyce, The evolving tumor microenvironment: from cancer initiation to metastatic outgrowth, Cancer Cell 41 (3) (2023) 374–403, https://doi.org/10.1016/j.ccell.2023.02.016.
[3] J. Huang, L. Zhang, D. Wan, L. Zhou, S. Zheng, S. Lin, et al., Extracellular matrix and its therapeutic potential for cancer treatment, Signal Transduct. Targeted Ther. 6 (1) (2021) 153, https://doi.org/10.1038/s41392-021-00544-0.
[4] F. Charbonier, M. Zamani, N. Huang, Endothelial cell mechanotransduction in the dynamic vascular environment, Adv. Biosyst. 3 (2018), https://doi.org/10.1002/adbi.201800252.
[5] C. Givens, E. Tzima, Endothelial mechanosignaling: does one sensor fit all? Antioxid. Redox Signaling 25 (7) (2016) 373–388, https://doi.org/10.1089/ars.2015.6493.
[6] Z. Yuan, Y. Li, S. Zhang, X. Wang, H. Dou, X. Yu, et al., Extracellular matrix remodeling in tumor progression and immune escape: from mechanisms to treatments, Mol. Cancer 22 (1) (2023) 48, https://doi.org/10.1186/s12943-023-01744-8.
[7] C. Ravelli, M. Corsini, R. Bresciani, A.M. Rizzo, L. Zammataro, P.A. Corsetto, et al., Cancer-associated VEGFR2, Neoplasia 67 (2025) 101195, https://doi.org/10.1016/j.neo.2025.101195.
[8] R.A. Toledo, E. Garralda, M. Mitsi, T. Pons, J. Monsech, E. Vega, et al., Exome sequencing of plasma DNA portrays the mutation landscape of colorectal cancer and discovers mutated VEGFR2 receptors as modulators of antiangiogenic therapies, Clin. Cancer Res. 24 (15) (2018) 3550–3559, https://doi.org/10.1158/1078-0432.ccr-18-0103.
[9] A. Benedetti, C. Turco, E. Gallo, T. Daralioti, A. Sacconi, C. Pulito, et al., ID4-dependent secretion of VEGFA enhances the invasion capability of breast cancer cells and activates YAP/TAZ via integrin β3-VEGFR2 interaction, Cell Death Dis. 15 (2) (2024) 113, https://doi.org/10.1038/s41419-024-06491-2.
[10] E. Grillo, C. Ravelli, M. Corsini, M. Domenichini, M. Scamozzi, D. Zizioli, et al., The expression level of VEGFR2 regulates mechanotransduction, tumor growth and metastasis of high grade serous ovarian cancer cells, Eur. J. Cell Biol. 103 (4) (2024) 151459, https://doi.org/10.1016/j.ejcb.2024.151459.
[11] M. Corsini, C. Ravelli, M. Domenichini, A. Ventura, C. Maggi, E. Moreschi, et al., Aberrant VEGFR2 supports tumor growth by extracellular matrix remodeling, Cell Death Dis. 17 (1) (2026) 169, https://doi.org/10.1038/s41419-025-08404-3.
[12] M.C. Farach-Carson, D. Wu, C.M. França, Proteoglycans in mechanobiology of tissues and organs: normal functions and mechanopathology, Proteoglycan Res. 2 (2) (2024), https://doi.org/10.1002/pgr2.21.
[13] Y. Wang, X. Wen, C. Su, Y. You, Z. Jiang, Q. Fan, et al., The role of tenascin-C in tumor microenvironments and its potential as a therapeutic target, Front. Cell Dev. Biol. 13 (2025) 1554312, https://doi.org/10.3389/fcell.2025.1554312.

[14] O. Hamza, A. Kiss, A.M. Kramer, S. Trojanek, D. Abraham, E. Acar, et al., Tenascin C promotes valvular remodeling in two large animal models of ischemic mitral regurgitation, Basic Res. Cardiol. 115 (6) (2020) 76, https://doi.org/10.1007/s00395-020-00837-5.
[15] K. Asano, C.M. Nelson, S. Nandadasa, N. Aramaki-Hattori, D.J. Lindner, T. Alban, et al., Stromal versican regulates tumor growth by promoting angiogenesis, Sci. Rep. 7 (1) (2017) 17225, https://doi.org/10.1038/s41598-017-17613-6.
[16] M. Nabi-Afjadi, F. Farzam, S. Soltani, N. Golestani, S.S. Asl, F. Aziziyan, et al., The association between periostin and tumor microenvironment: a promising cancer prognostic biomarker and therapeutic target to combat tumor progression and chemoresistance, Cancer Cell Int. 25 (1) (2025) 320, https://doi.org/10.1186/s12935-025-03959-9.
[17] D. Jeong, S. Ban, S. Oh, Lee S. Jin, Park S. Yong, Y.W. Koh, Prognostic significance of EDIL3 expression and correlation with mesenchymal phenotype and microvessel density in lung adenocarcinoma, Sci. Rep. 7 (1) (2017) 8649, https://doi.org/10.1038/s41598-017-08851-9.
[18] R.L. Huang, Z. Teo, H.C. Chong, P. Zhu, M.J. Tan, C.K. Tan, et al., ANGPTL4 modulates vascular junction integrity by integrin signaling and disruption of intercellular VE-cadherin and claudin-5 clusters, Blood 118 (14) (2011) 3990–4002, https://doi.org/10.1182/blood-2011-01-328716.
[19] Y. Wu, K. Zhang, J. Seong, J. Fan, S. Chien, Y. Wang, et al., In-situ coupling between kinase activities and protein dynamics within single focal adhesions, Sci. Rep. 6 (2016) 29377, https://doi.org/10.1038/srep29377.
[20] D. Mostert, J. Grolleman, M.C. van Turnhout, B.G.W. Groenen, V. Conte, C. M. Sahlgren, et al., SFAlab: image-based quantification of mechano-active ventral actin stress fibers in adherent cells, Front. Cell Dev. Biol. 11 (2023) 1267822, https://doi.org/10.3389/fcell.2023.1267822.
[21] J. James, L.B.A. Winn, P. Mottram-Epson, D. Köster, Paths to stability - actin regulation of adherens junction mechanics, J. Cell Sci. 138 (22) (2025), https://doi.org/10.1242/jcs.264055.
[22] M. Maupérin, Y. Sun, T. Glandorf, T.A. Oswald, N. Klatt, B. Geil, et al., A feedback circuitry involving γ-actin, β-actin and nonmuscle myosin-2 A controls tight junction and apical cortex mechanics, Nat. Commun. 16 (1) (2025) 2514, https://doi.org/10.1038/s41467-025-57428-y.
[23] V. Dugina, I. Zwaenepoel, G. Gabbiani, S. Clément, C. Chaponnier, Beta and gamma-cytoplasmic actins display distinct distribution and functional diversity, J. Cell Sci. 122 (Pt 16) (2009) 2980–2988, https://doi.org/10.1242/jcs.041970.
[24] V. Cheburkanov, V.V. Yakovlev, Brillouin microscopy analysis of the fibroblast mechanical response to substrate's stiffness, Soft Matter 21 (23) (2025) 4710–4718, https://doi.org/10.1039/d5sm00315f.
[25] N. Founounou, R. Farhadifar, G.M. Collu, U. Weber, M.J. Shelley, M. Mlodzik, Tissue fluidity mediated by adherens junction dynamics promotes planar cell polarity-driven ommatidial rotation, Nat. Commun. 12 (1) (2021) 6974, https://doi.org/10.1038/s41467-021-27253-0.
[26] R. Wakasugi, K. Suzuki, T. Kaneko-Kawano, Molecular mechanisms regulating vascular endothelial permeability, Int. J. Mol. Sci. 25 (12) (2024), https://doi.org/10.3390/ijms25126415.
[27] V.Z. Luu, B. Chowdhury, M. Al-Omran, D.A. Hess, S. Verma, Role of endothelial primary cilia as fluid mechanosensors on vascular health, Atherosclerosis 275 (2018) 196–204, https://doi.org/10.1016/j.atherosclerosis.2018.06.818.
[28] N. Ariyasinghe, J.P. Amoakon, A.P. Naren, Protocol for live-cell calcium imaging of human lung microvascular endothelial vessel-on-a-chip model, STAR Protoc. 6 (3) (2025) 104068, https://doi.org/10.1016/j.xpro.2025.104068.
[29] K.R. Molhoek, G. Erdag, J.K. Rasamny, C. Murphy, D. Deacon, J.W. Patterson, et al., VEGFR-2 expression in human melanoma: revised assessment, Int. J. Cancer 129 (12) (2011) 2807–2815, https://doi.org/10.1002/ijc.25963.
[30] Y. Wu, Y. Xu, Integrated bioinformatics analysis of expression and gene regulation network of COL12A1 in colorectal cancer, Cancer Med. 9 (13) (2020) 4743–4755, https://doi.org/10.1002/cam4.2899.
[31] E. Darang, Z. Pezeshkian, S.Z. Mirhoseini, S. Ghovvati, Bioinformatics and pathway enrichment analysis identified hub genes and potential biomarker for gastric cancer prognosis, Front. Oncol. 13 (2023) 1187521, https://doi.org/10.3389/fonc.2023.1187521.
[32] Z. Ma, C. Mao, Y. Jia, Y. Fu, W. Kong, Extracellular matrix dynamics in vascular remodeling, Am. J. Physiol. Cell Physiol. 319 (3) (2020) C481–C499, https://doi.org/10.1152/ajpcell.00147.2020.
[33] A. Mancini, M.T. Gentile, F. Pentimalli, S. Cortellino, M. Grieco, A. Giordano, Multiple aspects of matrix stiffness in cancer progression, Front. Oncol. 14 (2024) 1406644, https://doi.org/10.3389/fonc.2024.1406644.
[34] A.E. Mayorca-Guiliani, D.J. Leeming, K. Henriksen, J.H. Mortensen, S.H. Nielsen, Q.M. Anstee, et al., ECM formation and degradation during fibrosis, repair, and regeneration, NPJ Metab Health Dis. 3 (1) (2025) 25, https://doi.org/10.1038/s44324-025-00063-4.
[35] X. He, B. Lee, Y. Jiang, Extracellular matrix in cancer progression and therapy, Mediev. Rev. 2 (2) (2022) 125–139, https://doi.org/10.1515/mr-2021-0028.
[36] I. Klabukov, A.E. Kabakov, A. Yakimova, D. Baranovskii, D. Sosin, D. Atiakshin, et al., Tumor-Associated extracellular matrix obstacles for CAR-T cell therapy: approaches to overcoming, Curr. Oncol. 32 (2) (2025), https://doi.org/10.3390/curroncol32020079.
[37] M. Karsdal, T.R. Cox, A.L. Parker, N. Willumsen, J.M.B. Sand, G. Jenkins, et al., Advances in extracellular matrix-associated diagnostics and therapeutics, J. Clin. Med. 14 (6) (2025), https://doi.org/10.3390/jcm14061856.
[38] M.W. Parker, D. Rossi, M. Peterson, K. Smith, K. Sikström, E.S. White, et al., Fibrotic extracellular matrix activates a profibrotic positive feedback loop, J. Clin. Investig. 124 (4) (2014) 1622–1635, https://doi.org/10.1172/JCI71386.
[39] M. Fragiadaki, A.S. Witherden, T. Kaneko, S. Sonnylal, C.D. Pusey, G. Bou-Gharios, et al., Interstitial fibrosis is associated with increased COL1A2 transcription in AA-injured renal tubular epithelial cells in vivo, Matrix Biol. 30 (7–8) (2011) 396–403, https://doi.org/10.1016/j.matbio.2011.07.004.
[40] V. Sarohi, S. Chakraborty, T. Basak, Exploring the cardiac ECM during fibrosis: a new era with next-gen proteomics, Front. Mol. Biosci. 9 (2022) 1030226, https://doi.org/10.3389/fmolb.2022.1030226.
[41] M.T. Bu, P. Chandrasekhar, L. Ding, W. Hugo, The roles of TGF-β and VEGF pathways in the suppression of antitumor immunity in melanoma and other solid tumors, Pharmacol. Ther. 240 (2022) 108211, https://doi.org/10.1016/j.pharmthera.2022.108211.
[42] L. Li, Q. Wen, R. Ding, Therapeutic targeting of VEGF and/or TGF-β to enhance anti-PD-(L)1 therapy: the evidence from clinical trials, Front. Oncol. 12 (2022) 905520, https://doi.org/10.3389/fonc.2022.905520.
[43] L.A. Tomko, R.C. Hill, A. Barrett, J.M. Szulczewski, M.W. Conklin, K.W. Eliceiri, et al., Targeted matrisome analysis identifies thrombospondin-2 and tenascin-C in aligned collagen stroma from invasive breast carcinoma, Sci. Rep. 8 (1) (2018) 12941, https://doi.org/10.1038/s41598-018-31126-w.
[44] N. Bhola, S. Bhardwaj, C. Bareja, D. Saluja, Integrative analysis of angiogenesis-related genes highlights prognostic indicators in colorectal cancer through single-cell sequencing and immune infiltration analysis, Discov. Oncol. 16 (1) (2025) 1905, https://doi.org/10.1007/s12672-025-03614-9.
[45] A.K. Barry, N. Wang, D.E. Leckband, Local VE-cadherin mechanotransduction triggers long-ranged remodeling of endothelial monolayers, J. Cell Sci. 128 (7) (2015) 1341–1351, https://doi.org/10.1242/jcs.159954.
[46] M. Hirano, K. Hirano, Myosin di-phosphorylation and peripheral actin bundle formation as initial events during endothelial barrier disruption, Sci. Rep. 6 (2016) 20989, https://doi.org/10.1038/srep20989.
[47] H. Sun, J.W. Breslin, J. Zhu, S.Y. Yuan, M.H. Wu, Rho and ROCK signaling in VEGF-induced microvascular endothelial hyperpermeability, Microcirculation 13 (3) (2006) 237–247, https://doi.org/10.1080/10739680600556944.
[48] V.B. Dugina, G.S. Shagieva, A.S. Shakhov, I.B. Alieva, The cytoplasmic actins in the regulation of endothelial cell function, Int. J. Mol. Sci. 22 (15) (2021), https://doi.org/10.3390/ijms22157836.
[49] C. Handler, G. Zanini, I.M. Smith, K.M. Stroka, G. Scarcelli, C. Testi, Cellular mechanical properties in response to environmental viscosity imaged by Brillouin Microscopy, Commun. Biol. 8 (1) (2025) 1645, https://doi.org/10.1038/s42003-025-09032-5.
[50] Y.L. Dorland, S. Huveneers, Cell-cell junctional mechanotransduction in endothelial remodeling, Cell. Mol. Life Sci. 74 (2) (2017) 279–292, https://doi.org/10.1007/s00018-016-2325-8.
[51] J. Cao, H. Schnittler, Putting VE-cadherin into JAIL for junction remodeling, J. Cell Sci. 132 (1) (2019), https://doi.org/10.1242/jcs.222893.
[52] I.F. Hall, F. Kishta, Y. Xu, A.H. Baker, J.C. Kovacic, Endothelial to mesenchymal transition: at the axis of cardiovascular health and disease, Cardiovasc. Res. 120 (3) (2024) 223–236, https://doi.org/10.1093/cvr/cvae021.
[53] N. You, G. Liu, M. Yu, W. Chen, X. Fei, T. Sun, et al., Reconceptualizing endothelial-to-mesenchymal transition in atherosclerosis: signaling pathways and prospective targeting strategies, J. Adv. Res. 77 (2025) 419–441, https://doi.org/10.1016/j.jare.2024.12.049.
[54] J.S. Fang, N.W. Hultgren, C.C.W. Hughes, Regulation of partial and reversible endothelial-to-mesenchymal transition in angiogenesis, Front. Cell Dev. Biol. 9 (2021) 702021, https://doi.org/10.3389/fcell.2021.702021.
[55] S. Islam, K.I. Boström, D. Di Carlo, C.A. Simmons, Y. Tintut, Y. Yao, et al., The mechanobiology of endothelial-to-mesenchymal transition in cardiovascular disease, Front. Physiol. 12 (2021) 734215, https://doi.org/10.3389/fphys.2021.734215.
[56] H. Nakajima, K. Yamamoto, S. Agarwala, K. Terai, H. Fukui, S. Fukuhara, et al., Flow-Dependent endothelial YAP regulation contributes to vessel maintenance, Dev. Cell 40 (6) (2017), https://doi.org/10.1016/j.devcel.2017.02.019, 523-36.e6.
[57] K.J. Choi, J.K. Nam, J.H. Kim, S.H. Choi, Y.J. Lee, Endothelial-to-mesenchymal transition in anticancer therapy and normal tissue damage, Exp. Mol. Med. 52 (5) (2020) 781–792, https://doi.org/10.1038/s12276-020-0439-4.
[58] P. Leone, E. Malerba, N. Susca, E. Favoino, F. Perosa, G. Brunori, et al., Endothelial cells in tumor microenvironment: insights and perspectives, Front. Immunol. 15 (2024) 1367875, https://doi.org/10.3389/fimmu.2024.1367875.
[59] P. Carmeliet, R.K. Jain, Principles and mechanisms of vessel normalization for cancer and other angiogenic diseases, Nat. Rev. Drug Discov. 10 (6) (2011) 417–427, https://doi.org/10.1038/nrd3455.
[60] S. Guelfi, K. Hodivala-Dilke, G. Bergers, Targeting the tumour vasculature: from vessel destruction to promotion, Nat. Rev. Cancer 24 (10) (2024) 655–675, https://doi.org/10.1038/s41568-024-00736-0.
[61] H.T. Nia, L.L. Munn, R.K. Jain, Physical traits of cancer, Science 370 (6516) (2020), https://doi.org/10.1126/science.aaz0868.
[62] E. Grillo, M. Corsini, C. Ravelli, M. di Somma, L. Zammataro, E. Monti, et al., A novel variant of VEGFR2 identified by a pan-cancer screening of recurrent somatic mutations in the catalytic domain of tyrosine kinase receptors enhances tumor growth and metastasis, Cancer Lett. 496 (2021) 84–92, https://doi.org/10.1016/j.canlet.2020.09.027.
[63] C. Grashoff, B.D. Hoffman, M.D. Brenner, R. Zhou, M. Parsons, M.T. Yang, et al., Measuring mechanical tension across vinculin reveals regulation of focal adhesion dynamics, Nature 466 (7303) (2010) 263–266, https://doi.org/10.1038/nature09198.
[64] M. Jipp, B.D. Wagner, L. Egbringhoff, A. Teichmann, A. Rübeling, P. Nieschwitz, et al., Cell-substrate distance fluctuations of confluent cells enable fast and coherent

collective migration, Cell Rep. 43 (8) (2024) 114553, https://doi.org/10.1016/j.celrep.2024.114553.

[65] W. Giese, J.P. Albrecht, O. Oppenheim, E.B. Akmeriç, J. Kraxner, D. Schmidt, et al., Polarity-JaM: an image analysis toolbox for cell polarity, junction and morphology quantification, Nat. Commun. 16 (1) (2025) 1474, https://doi.org/10.1038/s41467-025-56643-x.

[66] K. Kartasalo, R.P. Pölönen, M. Ojala, J. Rasku, J. Lekkala, K. Aalto-Setälä, et al., CytoSpectre: a tool for spectral analysis of oriented structures on cellular and subcellular levels, BMC Bioinf. 16 (2015) 344, https://doi.org/10.1186/s12859-015-0782-y.